Special Issue on Remote Sensing - Monitoring for Urban Environment, 2nd Edition

PE&RS

April 2022 Volume 88, Number 4

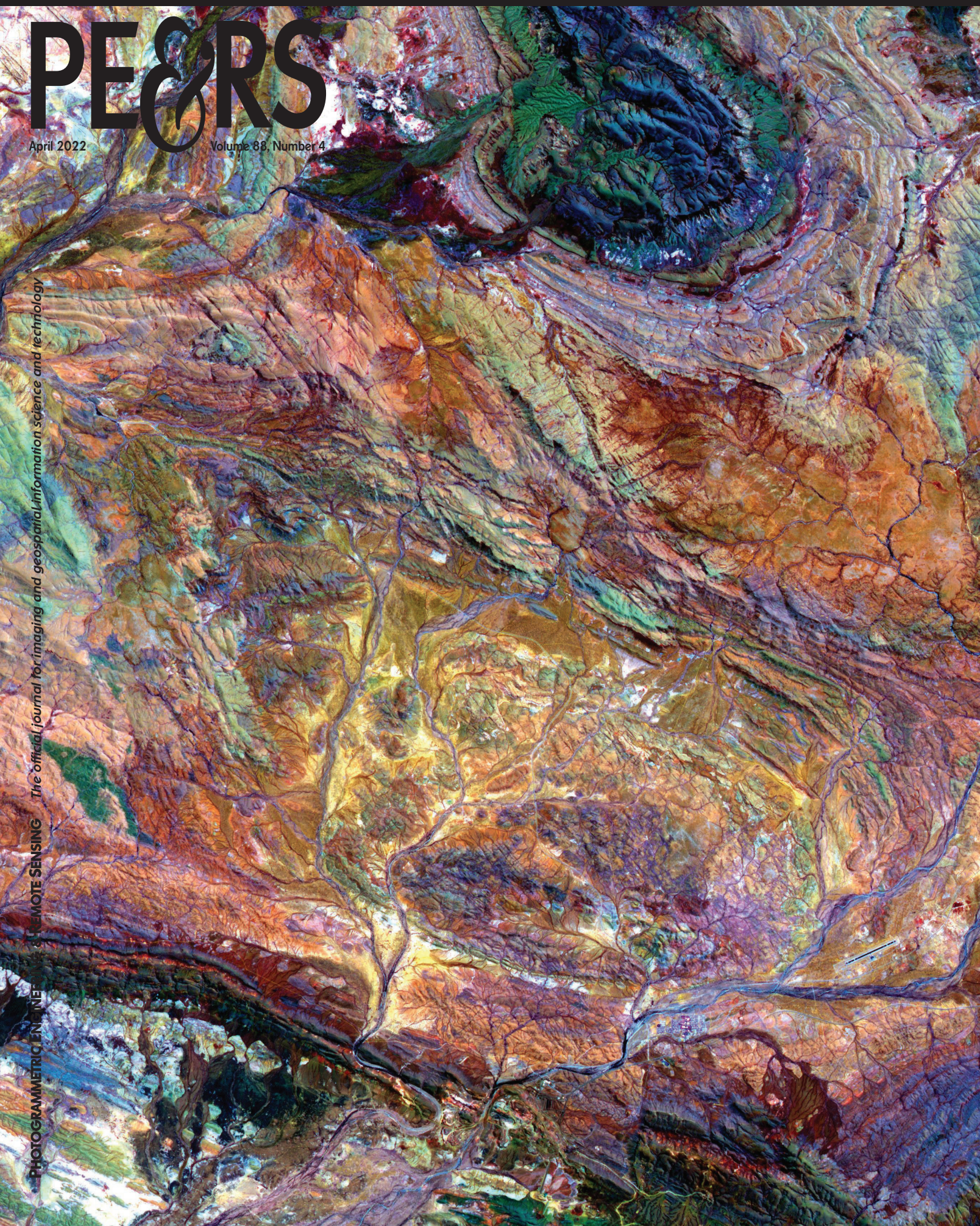

PHOTOGRAMMETRIC ENGINEERING & REMOTE SENSING The official journal for imaging and geospatial information science and technology

Landsat's Enduring Legacy

Pioneering Global Land Observations from Space

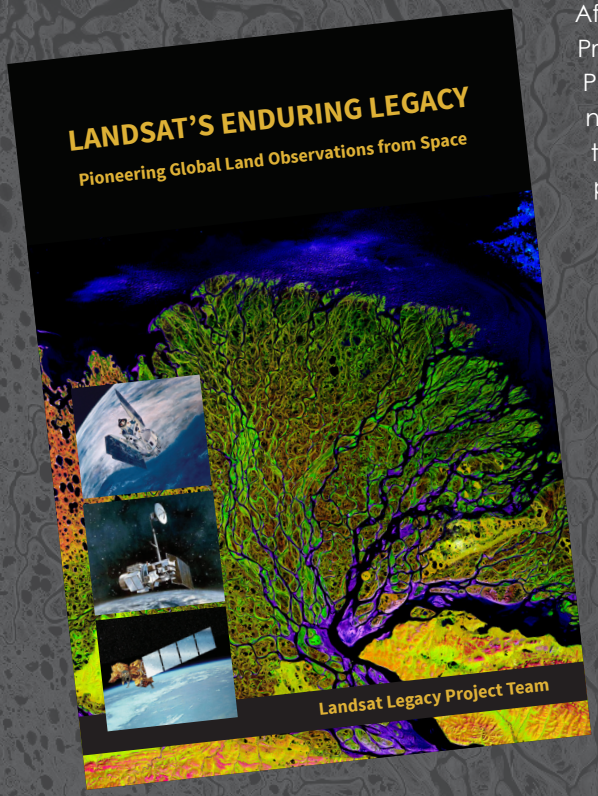

After more than 15 years of research and writing, the Landsat Legacy Project Team published, in collaboration with the American Society for Photogrammetry and Remote Sensing (ASPRS), a seminal work on the nearly half-century of monitoring the Earth's lands with Landsat. Born of technologies that evolved from the Second World War, Landsat not only pioneered global land monitoring but in the process drove innovation in digital imaging technologies and encouraged development of global imagery archives. Access to this imagery led to early breakthroughs in natural resources assessments, particularly for agriculture, forestry, and geology. The technical Landsat remote sensing revolution was not simple or straightforward. Early conflicts between civilian and defense satellite remote sensing users gave way to disagreements over whether the Landsat system should be a public service or a private enterprise. The failed attempts to privatize Landsat nearly led to its demise. Only the combined engagement of civilian and defense organizations ultimately saved this pioneer satellite land monitoring program. With the emergence of 21st century Earth system science research, the full value of the Landsat concept and its continuous 45-year global archive has been recognized and embraced. Discussion of Landsat's future continues but its heritage will not be forgotten.

The pioneering satellite system's vital history is captured in this notable volume on Landsat's Enduring Legacy.

Landsat Legacy Project Team

Samuel N. Goward
Darrel L. Williams
Terry Arvidson
Laura E. P. Rocchio
James R. Irons
Carol A. Russell
Shaida S. Johnston

Landsat's Enduring Legacy

Hardback. 2017, ISBN 1-57083-101-7

Student	$36*
Member	$48*
Non-member	$60*

* Plus shipping

Order online at

www.asprs.org/landsat

asprs THE IMAGING & GEOSPATIAL INFORMATION SOCIETY

ANNOUNCEMENTS

Teledyne Geospatial is pleased to announce that the next generation Optech CZMIL SuperNova topo/bathy lidar system has been awarded both the Geospatial Excellence Award for Technology Innovation and the Geospatial Excellence - Project of the Year Grand Award.

The Optech CZMIL SuperNova boasts the best depth performance and the highest green laser point density in its class. With SmartSpacing technology for even and efficient point spacing, real-time processing capability for reduced post-processing time and configurable modes for maximizing performance in different water environments, the SuperNova provides a wide range of inputs for climate change modelling and is Ideal for inland water environments, base mapping for coastal zones and shoreline.

A true geospatial solution, the CZMIL SuperNova's workflow is integrated with CARIS Base Editor software for seamless data processing capability and built-in AI techniques for land/water classification.

Teledyne Geospatial Director of Product Management Karen Cove comments, "We are thrilled to have the CZMIL SuperNova recognized by MAPPS and excited to see customers like Dewberry and Terratec tackle challenging projects with its demonstrated efficacy in environments like coastal beaches, inland waterways, coral reefs and deep-water mapping."

Teledyne Geospatial unifies the hardware and software expertise of both Teledyne CARIS and Teledyne Optech. The new group provides customers with innovative integrated solutions. Offerings include turnkey systems, lidar and sonar integrated workflows and a range of systems and solutions that support holistic, precision data collection.

NCEES seeks professional surveyors' and mapping scientists' expertise and advice NCEES is currently seeking licensed professional surveyors and mapping scientists to participate in a professional activities and knowledge study, or PAKS, for the Principles and Practice of Surveying (PS) exam. The results of this study will be used to update the specifications for the exam, which is used throughout the United States for licensing purposes.

NCEES requires a cross section of licensed professional surveyors and mapping scientists—including those working in consulting, the public sector, and academia—to complete an online questionnaire about the knowledge, skills, and abilities required of a newly licensed surveyor or mapping scientist to practice in a manner that safeguards the health, safety, and welfare of the public. The questionnaire can be completed in 35–45 minutes.

"These studies help NCEES ensure its licensing exams reflect current professional practice," explained Chief Officer of Examinations Jason J. Gamble, P.E. "We need input from as many professional surveyors and mapping scientists as possible to ensure that the PS exam continues to meet the demands of the profession."

For access to the online questionnaire, visit ncees.org/PSPAKS. Responses must be received no later than May 30, 2022. For more information, contact NCEES Exam Development Engineer John (Andy) Bindewald, P.E., at abindewald@ncees.org.

LAND INFO Worldwide Mapping LLC recently completed up-to-date 10m resolution thematic raster GIS data covering all 50 U.S. states. Optimized for low-band (broad-area coverage) 5G wireless planning, the dataset supports additional applications including utilities, insurance and government, and complements LAND INFO's 1m resolution datasets that are used for mid-band and high-band 5G in more densely populated areas.

"The dataset is unique in that in addition to using 2020-2021 Sentinel imagery and numerous ancillary layers, we were able to create best-in-class mapping by incorporating into our processing aerial-derived Digital Surface Model (DSM) elevation data via our longstanding partnership with Hexagon's HxGN Content Program," said LAND INFO president Nick Hubing.

The HxGN Content Program offers high-resolution, countrywide aerial imagery and elevation data of the contiguous United States and Western European countries. Hexagon continuously advances the program with higher resolution products for digital twin initiatives.

"We are proud to support LAND INFO's land-use/cover mapping solution with our high-quality DSMs," says John Welter, President, Geospatial Content Solutions at Hexagon. "LAND INFO is a well-established partner of Hexagon, and the partnership enables various industries to gain real-world analytics for reliable insights and better-informed decision making."

LAND INFO's proprietary automated geospatial processing technologies include object-based image analysis and artificial intelligence where smart rulesets analyzed, classified, and merged the imagery, DSM and ancillary layers into a single information rich dataset. There are currently just over 20 classes, and additional classes can be added upon request.

Visit www.landinfo.com for more information.

TECHNOLOGY

Phase One, a leading developer of digital imaging technologies, has announced its new iX Suite, a fully integrated software package for aerial mapping project management. Compatible with all Phase One PAS airborne systems, iX Suite handles mission planning, flight management, data acquisition, image selection and processing and in a common workflow.

"We developed the iX Suite for efficient collection and delivery of high-quality aerial image products," said Oodi Menaker, Phase One iX Suite Product Manager. "Every step of the workflow is planned and executed to ensure mapping projects are completed on time and on budget."

With the iX Suite, Phase One has taken a novel approach to managing aerial mapping projects by making quality control a key focus throughout the workflow to guarantee the generated image products meet end user specifications. A unique aspect of the iX Suite workflow is that imagery can be reviewed inflight and re-collected immediately if necessary, reducing the need for budget- and schedule-killing re-flights days or weeks later.

The iX Suite is comprised of three software tools that automate many functions to reduce workloads for pilots and operators in the air and streamline processing activities for technicians on the ground. These three software components are:

- iX Plan is a 3D photogrammetric flight planning application that takes end user requirements, terrain, and sensor properties into account to chart flightlines. The software includes a sensor database containing details of all Phase One PAS cameras and lidar sensors so that each image and point cloud acquisition is planned with exact area coverage, overlap, and resolution.
- iX Flight Pro is the flight and sensor management application that guides the pilot through the flight and triggers acquisition of sensor data. Images are displayed and overlaid on digital terrain model (DTM) in the graphical user interface so the onboard operator can view their quality and confirm precise coverage of the AOI.
- iX Process is an all-in-one mission review, quality assurance, and image export application. Using the mission report generated by iX Flight Pro, the processing tool overlays captured images on the flightline map and 3D DTMs, allowing the photogrammetric technician to check again for data quality and precise coverage of geographic areas. Accepted data sets are processed to generate and export images in commercial formats for delivery to end users.

"The iX Suite is tightly coupled with Phase One sensors, making our PAS aerial mapping systems easier, more intuitive, and cost-effective to operate," said Menaker. "Also, iX Suite interfaces with Riegl LiDAR systems, enabling customers to simultaneously operate a Phase One PAS camera and Riegl LiDAR with one management software in flight."

The Phase One PAS line of sensor systems was designed specifically to address the challenges of aerial image acquisition for 2D and 3D city modelling, photogrammetric mapping and surveying, agriculture, and other geospatial applications. The PAS product line includes the five-camera PAS 880 oblique and nadir system, PAS 280 large-format system, and PAS 150 systems.

Learn more at https://phaseone.ws/iX-suite.

CALENDAR

- 8 April, **ASPRS GeoByte—A History of the Landsat Program**. For more information, visit https://www.asprs.org/geobytes.html.
- 22 April, **ASPRS GeoByte— Using Geospatial Data to Evaluate Climate Hazards and Inform Environmental Justice**. For more information, visit https://www.asprs.org/geobytes.html.
- 27 May, **ASPRS GeoByte—Deep Fake Geography? A Humanistic GIS Reflection upon Geospatial Artificial Intelligence.** For more information, visit https://www.asprs.org/geobytes.html.
- 23 September, **ASPRS GeoByte— Allen Coral Atlas: A New Technology for Coral Reef Conservation.** For more information, visit https://www.asprs.org/geobytes.html.
- 3-6 October, **GIS-PRO 2022**, Boise, Idaho. For more information, visit https://www.urisa.org/gis-pro.
- 23-27 October, **Pecora 22**, Denver, Colorado. For more information, visit https://pecora22.org/.

PE&RS
PHOTOGRAMMETRIC ENGINEERING & REMOTE SENSING
The official journal for imaging and geospatial information science and technology
April 2022 Volume 88 Number 4

218 Resilient Research—Asking Students How the Pandemic has Impacted their Work, Strategies for Adaptation, and How SAC Can Help

COLUMNS

ANNOUNCEMENTS

Call for *PE&RS* Special Issue Submissions

DEPARTMENTS

See the Cover Description on Page 212

COVER DESCRIPTION

The Pilbara in northwestern Australia exposes some of the oldest rocks on Earth, over 3.6 billion years old. The iron-rich rocks formed before the presence of atmospheric oxygen, and life itself. Found upon these rocks are 3.45 billion-year-old fossil stromatolites, colonies of microbial cyanobacteria. The image, acquired in October 2004, is a composite of ASTER bands 4-2-1 displayed in RGB.

With its 14 spectral bands from the visible to the thermal infrared wavelength region and its high spatial resolution of about 50 to 300 feet (15 to 90 meters), ASTER images Earth to map and monitor the changing surface of our planet and is one of five Earth-observing instruments launched Dec. 18, 1999, on the Terra satellite. The instrument was built by Japan's Ministry of Economy, Trade and Industry. A joint U.S./Japan science team is responsible for validation and calibration of the instrument and data products.

The broad spectral coverage and high spectral resolution of ASTER provides scientists in numerous disciplines with critical information for surface mapping and monitoring of dynamic conditions and temporal change. Example applications are monitoring glacial advances and retreats; monitoring potentially active volcanoes; identifying crop stress; determining cloud morphology and physical properties; wetlands evaluation; thermal pollution monitoring; coral reef degradation; surface temperature mapping of soils and geology; and measuring surface heat balance.

Image Credit: NASA/METI/AIST/Japan Space Systems, and U.S./Japan ASTER Science Team.

For more information on this image, visit https://www.nasa.gov/image-feature/36-billion-years-in-pastel-colors.

PHOTOGRAMMETRIC ENGINEERING & REMOTE SENSING

JOURNAL STAFF

Publisher ASPRS
Editor-In-Chief Alper Yilmaz
Director of Publications Rae Kelley
Electronic Publications Manager/Graphic Artist
Matthew Austin

Photogrammetric Engineering & Remote Sensing is the official journal of the American Society for Photogrammetry and Remote Sensing. It is devoted to the exchange of ideas and information about the applications of photogrammetry, remote sensing, and geographic information systems. The technical activities of the Society are conducted through the following Technical Divisions: Geographic Information Systems, Photogrammetric Applications, Lidar, Primary Data Acquisition, Professional Practice, Remote Sensing Applications, and Unmanned Autonomous Systems Division. Additional information on the functioning of the Technical Divisions and the Society can be found in the Yearbook issue of *PE&RS*.

Correspondence relating to all business and editorial matters pertaining to this and other Society publications should be directed to the American Society for Photogrammetry and Remote Sensing, 8550 United Plaza Boulevard, Suite 1001, Baton Rouge, LA 70809, including inquiries, memberships, subscriptions, changes in address, manuscripts for publication, advertising, back issues, and publications. The telephone number of the Society Headquarters is 301-493-0290; the fax number is 225-408-4422; web address is www.asprs.org.

PE&RS. *PE&RS* (ISSN0099-1112) is published monthly by the American Society for Photogrammetry and Remote Sensing, 425 Barlow Place, Suite 210, Bethesda, Maryland 20814-2144. Periodicals postage paid at Bethesda, Maryland and at additional mailing offices.

SUBSCRIPTION. For the 2022 subscription year, ASPRS is offering two options to our *PE&RS* subscribers — an e-Subscription and the print edition. e-Subscribers can add printed copies to their subscriptions for a small additional charge. Print and Electronic subscriptions are on a calendar-year basis that runs from January through December. We recommend that customers who choose print and e-Subscription with print renew on a calendar-year basis.

The rate for a Print subscription for the USA is $1105.00 USD, for Canadian* is $1164.00 USD, and for Non-USA is $1235.00 USD.

The rate for e-Subscription (digital) Site License for the USA and Non-USA is $1040.00 USD and for Canadian* is $1089.00 USD.

The rate for e-Subscription (digital) plus Print for the USA is $1405.00 USD, for Canadian* is $1464.00 USD, and for Non-USA is $1435.00 USD.

*Note: e-Subscription, Print subscription, and e-Subscription plus Print for Canada includes 5% of the total amount for Canada's Goods and Services Tax (GST #135123065). **PLEASE NOTE: All Subscription Agencies receive a 20.00 USD discount.**

POSTMASTER. Send address changes to *PE&RS*, ASPRS Headquarters, 8550 United Plaza Boulevard, Suite 1001, Baton Rouge, LA 70809. CDN CPM #(40020812).

MEMBERSHIP. Membership is open to any person actively engaged in the practice of photogrammetry, photointerpretation, remote sensing and geographic information systems; or who by means of education or profession is interested in the application or development of these arts and sciences. Membership is for one year, with renewal based on the anniversary date of the month joined. Membership Dues include a 12-month electronic subscription to *PE&RS*. To receive a print copy of *PE&RS* there is an additional postage fee of $60.00 USD for U.S. shipping; $65.00 USD for Canadian shipping; or $75.00 USD for international shipping per year. Annual Individual Member dues for members residing in the U.S. and Other Foreign Members are $150.00 USD and $158.00 USD for Canadians. Annual Student Member dues for members residing in the U.S. are $50.00 USD; $53.00 USD for Canadian; and $60.00 USD for Other Foreign Members. A tax of 5% for Canada's Goods and Service Tax (GST #135123065) is applied to all members residing in Canada.

GIS Tips & Tricks

Savannah Carter & Al Karlin, Ph.D.
CMS-L, GISP

Need Help Finding GIS Tools – Here are a Few Tips

At some time, everyone comes to a point where they need help finding something that they know they have used before, but just cannot find. I frequently tell my students that "GOOGLE knows everything, so just ask GOOGLE!" GOOGLE is available 24/7 while I am available, hit or miss, so… What to do when GOOGLE cannot answer your question, or you know that you have used a GIS tool but just can't remember where to find it.

The solution is actually pretty simple, don't go to the "Help Menu"; use the Search functions. Here are some of Savannah's and my tips for (1) finding and (2) using the Search functions effectively.

For ArcGIS Desktop:

In ArcGIS Desktop there are multiple ways to open the Search functions. For those who prefer keyboard shortcuts, the <CTRL>-+F combination will open the search dialog box. For those who prefer mouse clicks, the Search dialog can be accessed from either the Geoprocessing tab (Figure 1) or the Windows tab (Figure 2) on the Main toolbar.

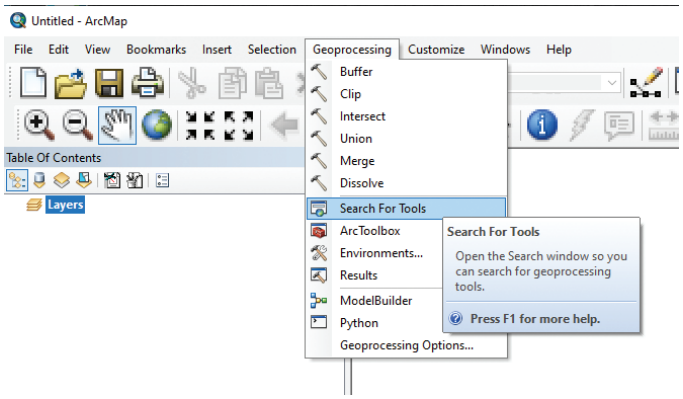

Figure 1. Accessing the Search functions from the Geoprocessing tab.

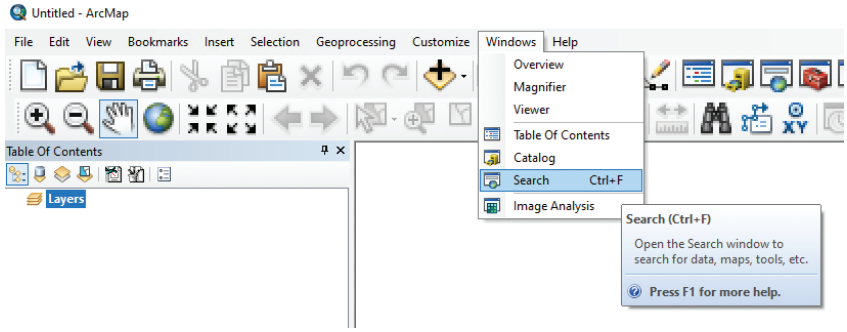

Figure 2. Accessing the Search functions from the Windows tab.

Once the Search dialog (Figure 3) opens, there are multiple tabs across the top to choose from for the search. Using the "All" tab will search for all objects in the ArcGIS environment containing the EXACT character string that you type. This can be extremely frustrating, particularly when you make a small typo (which we often do) as in the example in Figure 4, where a small typo, entering **raser** rather than **raster**, in the search yielded no results!

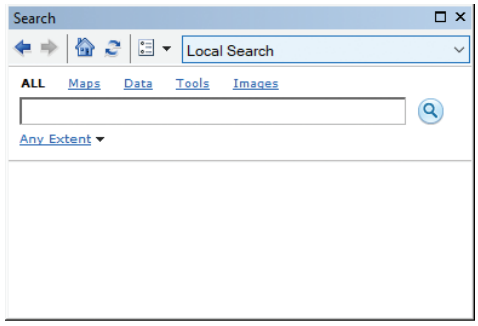

Figure 3. The Search dialog showing multiple tab filters acroass the top. The ALL filter tab is chosen in this example.

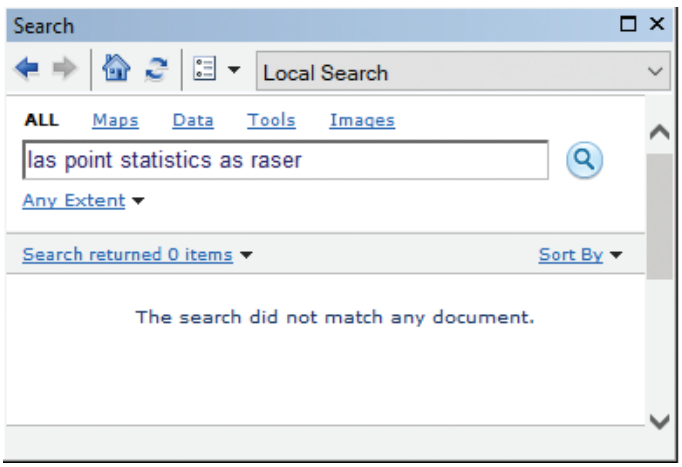

Figure 4. A small typo, raser instead of raster, in the search string failed to yield any results.

Photogrammetric Engineering & Remote Sensing
Vol. 88, No. 4, April 2022, pp. 213-215.
0099-1112/22/213-215

doi: 10.14358/PERS.88.4.213

When the typo was corrected, the search yielded the location to the desired tool as in Figure 5.

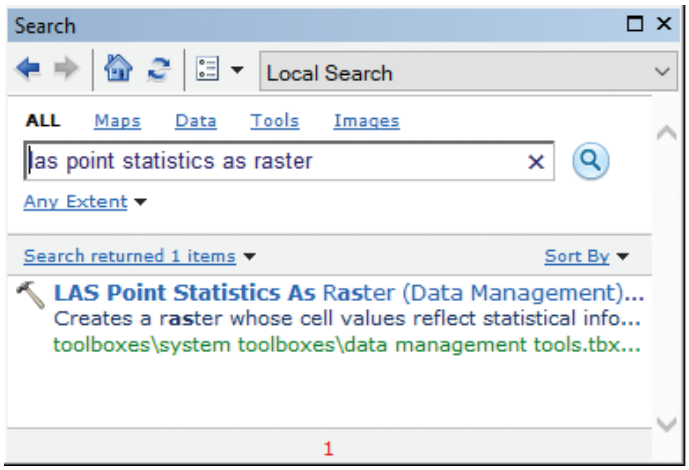

Figure 5. Correcting the typo, raster, not raser, in the search string yielded the desired tool.

TIP: An alternative is to search for tools using the Tool filter tab on the Search dialog. When using this tab, the search functions parses the search string as you type and offers suggestions to complete the string, as shown in Figure 6.

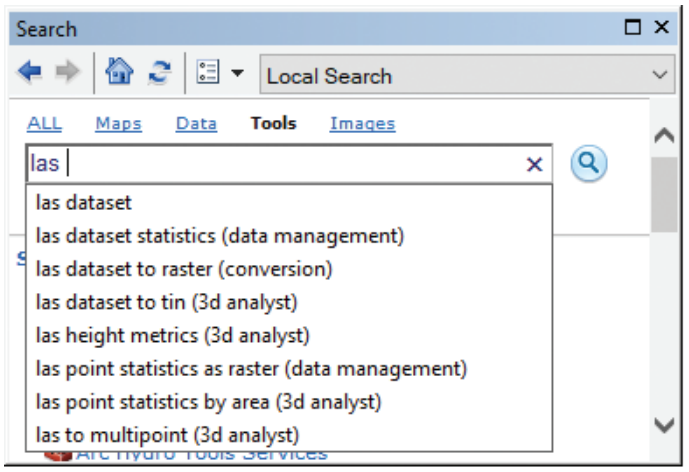

Figure 6. Using the Tools tab in the Search dialog box to search for tools.

For ArcGIS Pro

In ArcGIS Pro, the Geoprocessing tools are accessed through the "Analysis" Tab on the ribbon (Figure 7). Here, there are several "ready-to-use" tools and multiple ways to customize the tool groupings. But to search for a specific tool, clicking on the Tools icon will open the Geoprocessing dialog (Figure 8). Typing in the *Find Tools* box functions much like the ArcGIS Desktop search with the Tools filter and immediately starts to locate tools containing the character string and offers the options (Figure 9).

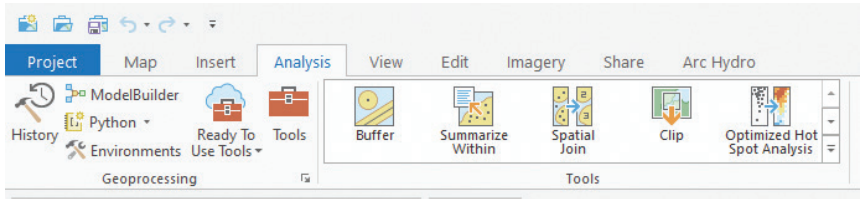

Figure 7. The "Tools" icon on the ArcGIS Pro Analysis Tab.

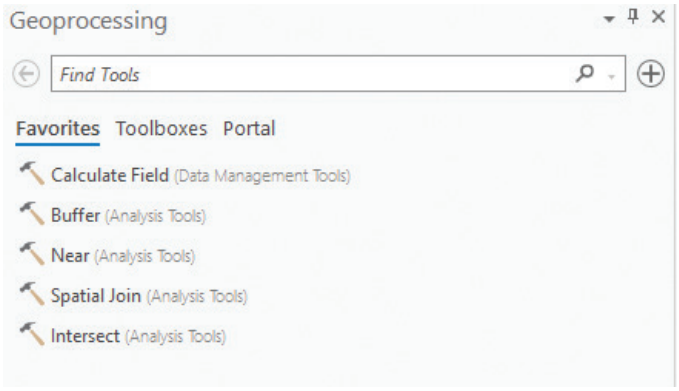

Figure 8. The Geoprocessing Dialog is used to Find Tools in ArcGIS Pro.

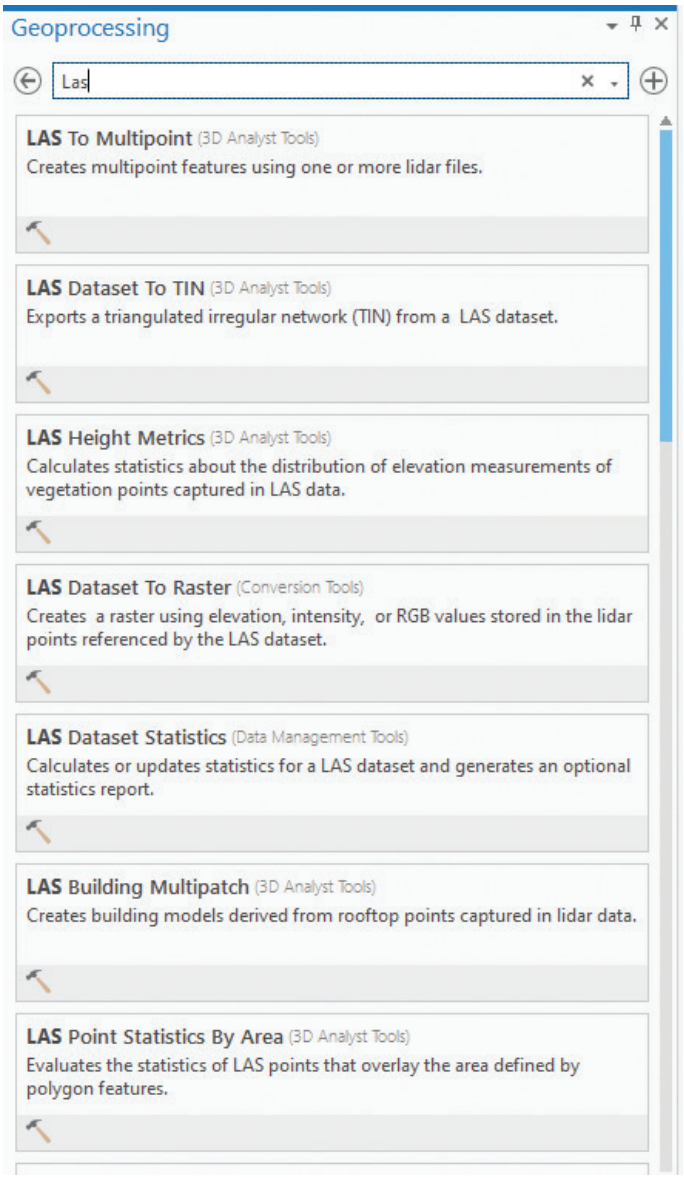

Figure 9. Typing in the Find Tools starts ArcGIS Pro to search for tools matching the character string while you type and offers list of tools to choose from.

In QGIS

In most versions of QGIS, the search for a processing tool is much the same as in ArcGIS Pro. The Processing Toolbox is opened from the Main Menu on the "Processing" tab as in Figure 10 or by the key combination <CTRL>+<ALT>+T.

Once the Processing Toolbox is opened, the search area at the top of the toolbox will initiate searching as you type. In the example below (Figure 11), I started typing "lidar", got as far as "lida" and the search engine suggested two raster and four vector tools, much like the ArcGIS Pro tool above. Double-clicking on a tool will open its dialog box.

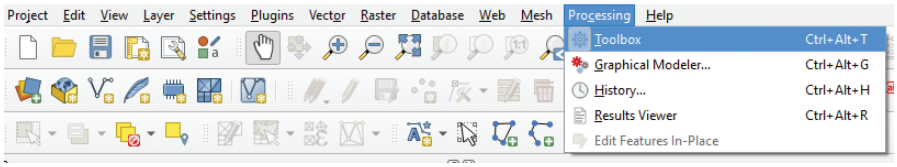

Figure10. QGIS Processing Tab opens the Toolbox.

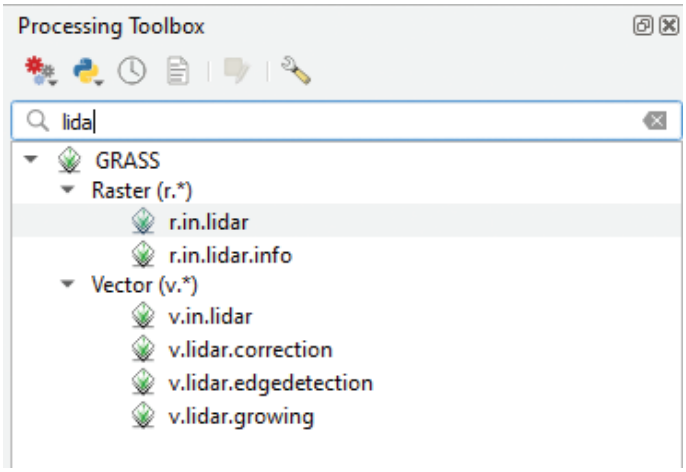

Figure 11. A search in QGIS for "lida" found 6 possible tools.

Not all GIS packages behave the way described above. In GlobalMapper the "Search" functions search for character strings in tables, names in files and/or geographic locations. So be aware of what your software does when you start searching.

Send your questions, comments, and tips to GISTT@ASPRS.org.

Savannah Carter is a Geospatial Analyst with Dewberry in the Tampa, FL office. She specializes in topographic and topobathymetric lidar data classification and interpretation Al Karlin, Ph.D., CMS-L, GISP is with Dewberry's Geospatial and Technology Services group in Tampa, FL. As a senior geospatial scientist, Al works with all aspects of Lidar, remote sensing, photogrammetry, and GIS-related projects.

& GRIDS & DATUMS

COMMONWEALTH OF THE BAHAMAS

BY Clifford J. Mugnier, CP, CMS, FASPRS

The Grids & Datums column has completed an exploration of every country on the Earth. For those who did not get to enjoy this world tour the first time, *PE&RS* is reprinting prior articles from the column. This month's article on the Commonwealth of the Bahamas was originally printed in 2004 but contains updates to their coordinate system since then.

Inhabited by Lucayan Indians at the time of sighting by Christopher Columbus on 12 October 1492, the islands were assigned to Spain by Papal grant. Subsequently occupied only by slave traders and buccaneers, the Bahamas were granted by the British Crown to Sir Robert Heath in 1629. The Commonwealth of the Bahamas became independent from the United Kingdom (*PE&RS,* October 2003) on 10 July 1973. Comprised of a 700-island and islet archipelago with an additional 2,400 cays and rocks in the North Atlantic Ocean, the total land area is 10,070 km^2, and it is slightly smaller than the State of Connecticut. With a total coastline of 3,542 km, the terrain of the Bahamas is primarily long, low coral formations with some low rounded hills. The lowest point is the Atlantic Ocean (sea level) and the highest point is Mount Alvernia (63 m) on Cat Island. Twenty-two of the main islands are inhabited; 70% of the population of 316,000+ live on New Providence, and 16% live on Grand Bahama.

Prior to World War II, the only surveys performed in the Bahamas were astronomical observations (Astros) of hazards to navigation and local cadastral-type surveys for some privately held properties. Initial geodetic ties of the islands to the mainland coast of Florida were performed with flare triangulations in the 1960s that were soon followed by BC-4 ballistic camera observations of the PAGEOS satellites. Flare triangulations were performed by simultaneous theodolite observations to parachute flares dropped from airplanes flying at high altitudes in order to make geodetic connections over the horizon. BC-4 observations were performed by photogrammetric triangulations of passive

satellite reflections against a background of star fields. Dr. Helmut Schmid (one of the original V-2 rocket scientists) led that geodetic program for the U.S. Coast & Geodetic Survey. The BC-4 program was the intercontinental geodetic program that tied all of the continents into the first worldwide geodetic system. Dr. Schmid was the designer of the BC-4 ballistic camera and was the mentor to Dr. Duane C. Brown, a pioneer of modern analytical photogrammetry. The Bahamas have been referenced to the North American Datum of 1927 (Clarke 1866 ellipsoid) since the 1960s, where a = 6,378,206.4 m and b = 6,356,583.8 m. The datum origin point is Meades Ranch, Kansas (quite a distance away) at: Φ_o= 39º 13′ 26.686″ N, Λ_o = –98º 32′ 30.506″ W., and the reference azimuth to station Waldo is α_o = 75º 28′ 09.64″ (*PE&RS*, April 2000).

Thanks to John W. Hager, the following positions have been determined in the Bahamas by classical observation techniques. These following geodetic positions (φ, λ) are presumably on the NAD27 while the astro positions (Φ, Λ) are

Photogrammetric Engineering & Remote Sensing
Vol. 88, No. 4, April 2022, pp. 216-218.
0099-1112/22/216-218

doi: 10.14358/PERS.88.4.216

independent: Elbow Cay Light (ECL), φ = 26° 32′ 21.715″ N, λ = –76° 57′ 10.870″ W. Also there is the Astro Observations (1940) where Φ = 26° 32′ 22.500″ N, Λ = –76° 57′ 15.353″ W, Astro Observations to light = 126.79 m, α = S 79° 01′ 27″ E true. Flamingo Cay Light (FLA), φ = 22° 52′ 43.48″ N, λ = –75° 51′ 38.28″ W. Great Inagua Island Light, φ = 20° 55′ 56.81″ N, λ = –73° 40′ 37.58″ W. Great Isaac Light (GIL), φ = 26° 01′ 48.30″ N, λ = –79° 05′ 22.08″ W. Great Ragged Island Light (GRL), φ = 22° 11′ 17.29″ N, λ = –75° 43′ 16.03″ W. Great Stirrup Cay (GSC), φ = 25° 49′ 36.41″ N, λ = –77° 53′ 50.20″ W. Gun Cay Light (GUN), φ = 25° 34′ 30.22″ N,λ = –79° 18′ 01.18″ W. Harvey Cay Light (HCL), φ = 24° 09′ 16.19″ N, λ = –76° 28′ 53.95″ W. Hog Island Light (HIL), φ = 25° 05′ 35.3″ N, λ = –77° 21′ 13.5″ W. Hogsty Reef Light (HRL), φ = 21° 41′ 27.71″ N, λ = –73° 50″ 56.81″ W. Hole-in-the-Wall Light (HIW), φ = 25° 51′ 32.522″ N, λ = –77° 10′ 37.938″ W. Observed astro (1940), Φ = 29° 51′ 22.320″ N, Λ = –77° 10′ 37.370″ W. Corrected in 1945, Φ = 29° 51′ 21.1155″ N, Λ = –77° 10′ 36.2901″ W. Little San Salvador Island (LIT), φ = 24° 33′ 53.73″ N, λ = –75° 56′ 08.00″ W. Man Island Light (MAN), φ = 25° 33′ 31.34″ N, λ = –76° 38′ 26.83″ W. Northwest Point Astro (NPA), Φ = 22° 27′ 24.42″ N, Λ = –73° 07′ 44.86″ W. Northwest Point Light (NPL), φ = 22° 27′ 35.56″ N, λ = –73° 07′ 47.43″ W. Pinder Point Light (PPL), φ = 26° 30′ 08.92″ N, λ = –78° 46′ 00.71″ W. Rum Cay Light (RUM), φ = 23° 38″ 36.1″ N., λ = –74° 50′ 05.7″ W. Santa Maria Light (SML), φ = 23° 40′ 54.54″ N., λ = –75° 20′ 27.60″ W. South Point Light (SPL), φ = 22° 50′ 56.48″ N., λ = 74° 51′ 14.42″ W. Stocking Island Astro (SIA), Φ = 23° 32′ 33.97″ N., Λ = –75° 46′ 10.75″ W. Sweetings Cay Light (SWC), φ = 26° 36′ 40.62″ N., λ = –77° 54′ 00.86″ W.

The NGA lists the three-parameter transformation from NAD27 to WGS84 for the Bahamas excluding San Salvador Island as ΔX = –4 m±5 m, ΔY = +154 m ±3 m, and ΔZ = +178 m ±5 m, where the 1987 solution is based on 11 station observations. For San Salvador Island, ΔX = +1 m ±25 m, ΔY = +140 m ±25 m, and ΔZ = +165 m ±25 m, and the 1987 solution is based on one station observation. In 1997, the U.S. National Geodetic Survey observed a number of high-order positions in the Bahamas on the NAD83 datum. The only grid ever used in the Bahamas is the UTM.

The Commonwealth of the Bahamas Update

The U.S. Department of State issued a new paper on Limits in the Seas, No. 128 on the Bahamas Archipelagic and other Maritime Claims and Boundaries on 31 January 2014. "This study analyzes the maritime claims and maritime boundaries of the Commonwealth of The Bahamas, including its archipelagic baseline claim. The Bahamas' Archipelagic Waters and Maritime Jurisdiction (Archipelagic Baselines) Order, 2008 (Annex 1 to this study) took effect on December 8, 2008 and established the coordinates for the archipelagic baselines of The Bahamas.1 The archipelagic baselines are shown on Map 1 to this study. This Order was made in exercise of the powers conferred by section 3.2 of the Archipelagic Waters and Maritime Jurisdiction Act, 1993 (Act No. 37, Annex 2 to this study).2 The 1993 Act also established a 12- nautical mile (nm) territorial sea and 200-nm exclusive economic zone (EEZ). The Bahamas ratified the 1982 United Nations Convention on the Law of the Sea (LOS Convention) on July 29, 1983 and consented to be bound by the 1994 Agreement Relating to the Implementation of Part XI of the Convention on July 28, 1995.3." http://www.state.gov/e/oes/ocns/opa/c16065.htm.

The contents of this column reflect the views of the author, who is responsible for the facts and accuracy of the data presented herein. The contents do not necessarily reflect the official views or policies of the American Society for Photogrammetry and Remote Sensing and/or the Louisiana State University Center for GeoInformatics (C^4G).

This column was previously published in *PE&RS*.

asprs THE IMAGING & GEOSPATIAL INFORMATION SOCIETY
STUDENT ADVISORY COUNCIL

THE ASPRS STUDENT ADVISORY COUNCIL (SAC)

Resilient Research—Asking Students How the Pandemic has Impacted their Work, Strategies for Adaptation, and How SAC Can Help.

It has been a tough two years. The pandemic has dramatically changed many aspects of our lives, and the future remains uncertain. Though our individual experiences may differ, we at SAC feel that it is important that every person in our community (geospatial and beyond) knows that they are not alone. We feel that it is essential for all of us to pause and reflect on the emotional and physical toll of these past two years. This processing is not meant to simply be a rehashing of difficult times but is instead intended to help us respect where we have been, so we can understand how to continue on to a path of healing and growth.

For this special edition of SAC Signatures, the SAC team reached out to students asking them about their experiences conducting research during the COVID-19 pandemic and requested that they share any advice for other students experiencing similar issues. Finally, we asked them to share how SAC has helped or can continue to help them meet their goals and provide continued support. The responses we received touched on all spheres of student life (work, home, and social aspects), helping us to better understand that vast ripple effects caused by the pandemic, and how these effects interact and interfere with research and study.

Student Responses

1. **How did the COVID-19 pandemic affect the progress of your research?** *Answers are summarized by category.*

   - **Data Collection & Analysis**
     Unsurprisingly, a big impact of the pandemic was inability to conduct field work and collect data or in-person interviews. Furthermore, students noted that fulfilling deadlines was more difficult as they struggled to meet with peers and advisors. Communication, though possible through zoom, was lacking for some students compared to meeting in person.

   - **Technology & Education**
     During the pandemic, access to school technology has been limited, forcing students to use their own internet and computers. This has proved difficult for some with limited WIFI or computers that are not as powerful as those at school. As classes became fully remote, some students felt lapsing engagement with class content.

   - **Social Life & Wellbeing**
     Students reflected on how seeing the global and local impacts of COVID-19 (or even catching it themselves) has been a big source of stress and anxiety. Further, students reflected on how the pandemic has inequitably impacted caregivers who must juggle work and family life as well as the experiences of those who are, or are caring for, immunocompromised individuals. As social gatherings became impossible and public places closed, students felt isolated. Though these in-person gatherings were often replaced with virtual ones, students experienced a new issue: "zoom burn out", where endless virtual meetings became somewhat draining. Additionally, students discussed the physical impacts of working from home, including pains and stiffness from sitting at a desk all day

Pandemic Research Impacts.

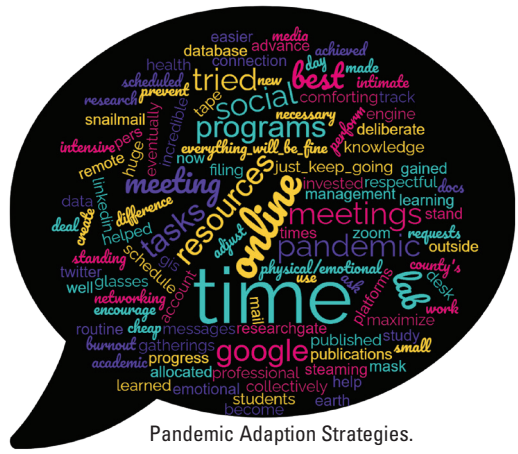

Pandemic Adaption Strategies.

2. **What strategies did you use to adapt to the impacts of the pandemic? What advice do you have for students conducting research during the pandemic?** *Answers are summarized by category.*

   - **Data Collection & Analysis**
     Students suggest using professional social networks, such as LinkedIn, ResearchGate, and others to expand their professional networks and learn about exciting new skills and data resources.
   - **Technology & Education**
     For collaborative projects and assignments, students recommend using resources like Google Docs, as these make it easier to work together and track progress. Students also stress the importance of time management to stay productive while working remotely.
   - **Social Life & Wellbeing**
     To ease isolation, students suggest using "snail mail" to correspond with friends and family and to, when safe to do so, hold small gatherings for social or study time. To help with mental and physical health, scheduling and regularly taking walks was suggested (as well as investment into a cheap standing desk). Another bit of advice for our bespectacled community members was to tape your mask across your nose to prevent your glasses steaming up. Finally, students remind us to keep going and remember that "everything will be fine".

3. **How did engagement in SAC and ASPRS assist you in achieving your professional and academic goals during the pandemic? What else can SAC do to support you?**
   Students shared their gratitude for the professional, academic, and social connections SAC strives to provide to students. Furthermore, students are grateful for the opportunities shared and implemented by ASPRS, such as scholarships, events, and space to present their work. Students also expressed appreciation for the connection and resources provided by their local ASPRS student chapters. SAC will work hard to continue to share resources for students and make space for collaboration and networking. **Thank you to all the students who participated in our survey!**

How SAC and ASPRS have helped.

If you are interested in participating in SAC activities

- Join us every other Thursday from 10-11 am PST!
- Join us via this zoom link, https://tinyurl.com/SACASPRSMeeting

Call for *PE&RS* Special Issue Submissions

Multimodal Remote Sensing Data Processing and Analysis for Earth Observation

Earth observation, by providing critical information on natural resources, hazardous areas, and climate change, among others, is a powerful tool in all aspects of life. The observations come primarily from space-based sensors such as satellites, but they highly depend on ground-based remote sensing devices. Multimodal remote sensing systems integrate optical and passive microwave radiometers to improve the quality of observations. The versatility of multimodal RS offers enormous potential to monitor diverse target phenomena in all climate system components with high spatial, temporal, or spectral resolution. It provides innovative methods for processing multispectral, hyperspectral, and polarimetric remote sensing data for different vegetation, geophysical, and atmospheric applications to understand the earth better. However, there are still challenges to achieving maximum exploitation of multimodal data. At the same time, the combination of multimodal remote sensing technologies is a powerful approach that can yield significant advantages compared to traditional single-modal sensors.

The techniques such as image processing is typically used to adjust and refine data derived from remote sensing. Its capabilities are also useful for merging data sources. Image processing techniques, such as filtering and feature extraction, are well suited for dealing with the high-dimensionality of spatially distributed systems. The input data may come from different sensors, each with a different spatial resolution and measurement scale ('multimodal'). It provides approaches for the extraction of relevant non-topographic information from remote sensing data, such as demographic indicators from satellite images of urban areas, which could assist in future spatial modelling of these areas. It helps to analyze shape, topography, and texture phenomena for soil and vegetation data and various methods for image fusion and analysis of the optical, radar, and gravity data. It covers a wide range of geospatial applications, including land and water resources management, urban planning, environmental monitoring, natural hazards and climate change, oceanography, engineering design, and national security and intelligence. It processes multispectral, thematic-mapping, thermal-infrared (TIR), hyperspectral data acquired from optical, SAR or lidar platforms with advanced techniques in the areas of scene characterization and feature extraction.

This special issue is intended for remote sensing scientists, engineers, and researchers involved in its application for earth observation. Innovative techniques dealing with climate monitoring; environmental monitoring, including pollution monitoring and deforestation detection; geographical information system (GIS) applications; maps generation, land cover classification and change detection; mineral exploration industries; hydrology and water resources management; based on multimodal remote sensing data are most invited for submission.

List of Topics (include, but not limited to the following):

- Deep learning and computer vision for earth observation and multimodal remote sensing
- Semantic and instance segmentation of the multimodal remote sensing data for earth observation and analysis
- Multimodal remote sensing data fusion, interpretation and analysis for earth observation
- Hyperspectral remote sensing and image processing for earth observation
- Light weight deep neural network algorithms for earth surveillance
- Earth object classification and recognition using multimodal remote sensing approaches
- Multi-resolution and multi-modal remote sensing for enhancing the earth observation processes
- Novel applications of multi-modal remote sensing in earth monitoring and surveillance processes
- Spatio-temporal data analysis for efficient earth observation
- Multimodal data reconstruction and restoration for efficient classification process
- Benchmarking multimodal datasets for earth observation
- New algorithms and frameworks for efficient analysis of multimodal remote sensing data

Deadline for Manuscript Submission
August 1, 2022

Submit your Manuscript to
http://asprs-pers.edmgr.com

Guest Editors

Dr. Ahmed A. Abd El-Latif, alatif@science.menofia.edu.eg, Associate Professor, *Department of Mathematics and Computer Science, Faculty of Science, Menoufia University*, Egypt.

Dr. Edmond Shu-lim Ho, e.ho@northumbria.ac.uk, Senior Lecturer, *Department of Computer and Information Sciences, Northumbria University, Newcastle upon Tyne*, United Kingdom.

Dr. Jialiang Peng, jialiangpeng@hlju.edu.cn, Associate Professor, *School of Data Science and Technology, Heilongjiang University*, China.

ASPRS ANNOUNCES UPCOMING GEOBYTES!

A History of the Landsat Program
Presented by Ellie Leydsman McGinty, *AmericaView*
April 8th

Using Geospatial Data to Evaluate Climate Hazards and Inform Environmental Justice
Presented by Carolynne Hultquist and Cascade Tuholske, *Center for International Earth Science Information Network*
April 22nd

Deep Fake Geography? A Humanistic GIS Reflection upon Geospatial Artificial Intelligence
Presented by Dr. Bo Zhao, *University of Washington, Seattle*
May 27th

Allen Coral Atlas: A New Technology for Coral Reef Conservation
Presented by Brianna Bambic, N*ational Geographic Society and Arizona State University*
September 23rd

For complete details and to register, visit https://www.asprs.org/geobytes.html.

NEW ASPRS MEMBERS

ASPRS would like to welcome the following new members!

Matilda Anokye
Caroline Yeboaa Apraku
Recheal Naa Dedei Armah
Julia Atayi
Kajetan Bauer
Austin M. Breunig
Aaron T. Brown
Richard Butkus, III
Marshall Edens
Jordan Edmunds
Abdelgwad Elashry
Jacob Freeman
Jedidiah Gibson, PLS
Francisco Joseph Gonzales
Jonathan Haislip
Miranda Hechler
Mackenzie Higgins
Lashunda Anderson Hodges, PhD
Eric James Householder, GISP
Nathan Jones
Joshua King
Fritz Koether
John P. Lynch, PLS
Justin Yancey Morgan
Maung Moe Myint, PhD
Leyla Namazie
Allen Paton
Pratikshya Regmi
Pamela Ann Rodriguez
Molly Colette Smith
Dan Staley
Elizabeth Stockwell
David Strohschein, Ph.D.
Stewart Walden
Jeremy W. Whitefoot
Don Widener, PhD

FOR MORE INFORMATION ON ASPRS MEMBERSHIP, VISIT
HTTP://WWW.ASPRS.ORG/JOIN-NOW

Call for *PE&RS* Special Issue Submissions

Modelling, Representation, and Visualization of the Remote Sensing Data for Forestry Management

Remote sensing data includes aerial photography, videography data, multispectral scanner (MSS), Radar, and laser to map and understand various forest cover types and features. An accurate digital model of a selected forest type is developed using forest inventory data in educational and experimental forestry and extensive databases. It includes the formalization and compilation of methods for integrating forest inventory databases and remote sensing data with three-dimensional models for a dynamic display of forest changes.

Big data technology employs vast amounts of forestry data for forestry applications that require real-time inquiry and calculation. The techniques and strategies of forestry data analysis are integrated into the big data forestry framework, enabling interfaces that other Programmes may call. Virtual Reality addresses constraints in forest management such as temporal dependence, irreversibility of decisions, spatial-quantitative change of characteristics, and numerous objectives. Virtual representations integrate various computer graphics systems with display and interface devices to create a spatial presence in an interactive 3 D environment. Visualization of plant species' growth patterns, changes in species and their composition, and other morphological properties of forests are enhanced using machine learning and regression analysis methods as part of a digital model. In modelling, deep learning (DL) replicates expert observations on hundreds or thousands of hectares of trees.

Remote sensing is being used to map the distribution of forest resources, global changes in flora with the seasonal variations, and the 3D structure of forests. Graphic Information System (GIS) based visualizations depict dynamics through animations and 3D geo model visualizations and allow advanced spatial analytics and modelling in geographical phenomena for forest management. Digital forest modelling includes integrating forest inventory data, forest inventory database formation, graphics objects of forest inventory allocations with a digital forest model, and technology for visualizing forest inventory data. It helps forecast changes and visualizes situational phenomena occurring in forests using data and models involving spatial-temporal linkages.

Standard aerial shots capture images that view unseen components to the naked eye, such as the Earth's surface's physical structure and chemical composition. The challenges in remote sensing models include insufficient Remote Sensing (RS), spatial, spectral, and temporal resolution to detect degradation accurately. High costs of RS, the gap between operational and scientific uses, and lack of information sharing are some of the challenges of RS for forest management. The list of topics of interest include but are not limited to the following:

- Advancement of forest surveillance through Geographical Information Systems
- State of the art and perspectives of modelling and visualization framework for Forest type mapping and assessment of distribution
- Futuristic Satellite data analysis for stock maps and forest inventory analysis
- Big data-enabled GIS framework for forest management information
- AI-based Space Remote Sensing For Forest Ecosystem Assessment
- Enhanced visualization through deep learning for forest management solutions
- Novel approaches of multi-temporal satellite data using digital image analysis for forest management
- Advance representation of discrete objects and continuous fields in virtual environments through VR framework
- Database framework for regional and plot-based forest allotment data for model representation and visualization
- Development of scalable models for area-based metrics from Light Detection and Ranging (lidar) devices and photographic structure-for-motion (SFM)

Deadline for Manuscript Submission—June 7, 2022

Submit your Manuscript to http://asprs-pers.edmgr.com

Guest Editors

Dr. Gai-Ge Wang, gai-gewang@outlook.com and wgg@ouc.edu.cn, *Department of Computer Science and Technology, Ocean University of China*, China

Dr. Xiao-Zhi Gao, xiao.z.gao@gmail.com and xiao-zhi.gao@uef.fi, *Machine Vision and Pattern Recognition Laboratory, School of Engineering Science, Lappeenranta University of Technology*, Finland.

Dr. Yan Pei, peiyan@u-aizu.ac.jp, *Computer Science Division, The University of Aizu*, Japan.

Research on Machine Intelligent Perception of Urban Geographic Location Based on High Resolution Remote Sensing Images

Jun Chen, Cunjian Yang, and Zhengyang Yu

Abstract

Machine intelligent perception (MIP) provides a novel way for human beings to recognize geographical locations automatically. MIP *of geographical locations enables computers to describe locations automatically and quantitatively by extracting Earth's surface features and building relationships. The earth surface fingerprint is established here by mining the relationship between spatial objects with stable characteristics extracted from urban high-resolution remote sensing images, which realizes intelligent perception of geographical location innovatively. Mask Region-based Convolutional Neural Network is used to automatically extract the spatial objects such as playgrounds, crossroads, and bridges from the images. Then, the extracted spatial objects are encoded according to the landuse type, distance, and angle of 24 nearest objects to construct urban surface fingerprint database. The urban surface fingerprint database is used to match the geographical location of spatial objects in local images so that the matching algorithm can be used for machine recognition of the geographical location of specific objects in the target image. Taking the main cities in China as the experimental area, the success rate of location perception is 92%. We have made a useful exploration in the field of MIP of geographical location, hoping to promote the development of human cognition of geographical location.*

Introduction

Human cognition of geographical location has gone through four stages. Before words appeared, people expressed geographical location by tying knots on ropes. After the invention of words, people began to record geographical location with words. Later, people learned to represent locations by drawing maps, and the appearance of maps is a great leap in human cognition of geographical location. With the advent of computers, geographical location is digitized, so the calculation and service based on geographical location can be provided by computers. Today, cutting-edge technologies such as high-performance computing and artificial intelligence constantly stimulate and give birth to new demands and new applications. The machine intelligent perception (MIP) of geographical locations is a new stage of human cognition of geographical locations and is an important frontier topic in geographic information science.

The key to MIP of a geographical location is to establish a set of methods so that computers can describe the location automatically and quantitatively. At present, it mainly involves two areas of research: one is based on the image features, and the other is to establish the concept of geo-science mapping to understand geographic location. The former determines the features contained in the image through various transformations, and then realizes geographic location perception by using the feature matching algorithm (Jiang *et al.* 2021). The classical methods for automatically extracting features include Harris feature (Kovacs and Sziranyi 2013; Vishwakarma and Bhuyan 2020; Wang *et al.* 2008), scale-invariant feature transform (SIFT) feature (Yang *et al.* 2019; Yao *et al.* 2009; Zhou 2009) and speeded up robust features (SURF) feature (Bay *et al.* 2006; Su *et al.* 2010; Tong *et al.* 2021). With the improvement of algorithms, the accuracy and efficiency of feature extraction are getting higher and higher. For example, Rublee *et al.* proposed an improved ORB model, which is rotation invariant and resistant to noise (Rublee *et al.* 2011). Wu adopted a feature detection method based on image grayscale information-FAST operator to improve the speed of extracting image feature points (Wu 2019). However, due to the limitation of algorithms, a large number of feature points are often extracted from an image. So, it requires a complex algorithm to extract useful information that can distinguish specific geographical locations from a large number of feature points. Fan and Zhao proposed a matching process to cluster features from a group of reference images in order to enhance matching robustness (Fan and Zhao 2012). Liu *et al.* proposed a simple and robust feature point matching algorithm, called Restricted Spatial Order Constraints (RSOC), to remove outliers for registering aerial images with monotonous backgrounds, similar patterns, low overlapping areas, and large affine transformation (Liu *et al.* 2012). Chen *et al.* proposed a line-based matching method to overcome the low significant level of point feature and the shortage in the matching between weak texture images (Chen *et al.* 2013). Although some progress has been made in feature screening and matching optimization, for machine intelligent sensing location, it is necessary to analyze a wide range of remote sensing images and extract a small number of evenly distributed features to quickly indicate the location of any place in the region. The existing research rarely involves this field. Due to the complexity of algorithm and data organization, it is difficult to directly migrate to the field of MIP of geographical location.

Geo-science mapping is another prospective study in this field. Based on the theory of geo-science mapping, Luo proposed the spatial cognition theory coupled with remote sensing mapping and constructed a theoretical and methodological system in the way of "pixel-object-object-pattern" (Matsuoka and Midorikawa 1993). Based on the theory of geo-science mapping and geographic information systems (GIS) technology, Lu analyzed the land use "pattern map", "classification map", "transfer map", "change pattern map", and "fluctuation map" of land border areas of Guangxi Province from 2003 to 2013, and thus revealed the spatial-temporal evolution process of land use (Rucheng *et al.* 2009). Abrams (2017) constructed the geo-science mapping of the land surface. Hewson's project demonstrated, within the study areas of Wagga and Cobar, the usefulness of the National ASTER Geoscience Map products for identifying variations in the composition of surface materials (Hewson and Robson 2014). Moosavi proposed a generic

Jun Chen and Zhengyang Yu are with Chengdu University of Information Technology, Chengdu, China (494834920@qq.com).

Cunjian Yang is with 1. Key Laboratory of Land Resources Evaluation and Monitoring in Southwest, Ministry of Education, Sichuan Normal University; 2. Research Center of Remote Sensing and Geographic Information System Application,The College of Geography and Resource Sciences,Sichuan Normal University.

Contributed by Zhenfeng Shao, April 14, 2021 (sent for review October 8, 2021; reviewed by Bin Hu, Hongping Zhang).

Photogrammetric Engineering & Remote Sensing
Vol. 88, No. 4, April 2022, pp. 223–231.
0099-1112/22/223–231

doi: 10.14358/PERS.21-00017R3

methodology for combining high-dimensional spatial data to identify and visualize the hidden spatial patterns in a single-layer geo-map (Moosavi 2017). At present, the study of geo-science mapping is still in its infancy, and different scholars describe geographical features in a different way, so it is difficult to establish a unified index to automatically construct regional geo-science mapping.

The realization of MIP of geographical location needs to be completed automatically by the computer. Given the current research results, there is still a long way to go. This paper, with cities as the research area, tries to introduce the concept of surface fingerprint, discusses how to make computers automatically extract objects from remote sensing images, and establishes surface fingerprints. By doing so, it realizes the preliminary MIP of geographical location.

The Concept of Machine Perception of Geographical Location

Surface Fingerprint

Fingerprint, also called handprint, is characterized by raised lines on the epidermis. Human fingerprint is the product of a combination of environmental and genetic factors. Everyone has unique fingerprints. Fingerprint lines are not smooth or continuous, and the interruptions, bifurcations, or turns, as feature points, are the basis of fingerprint identification.

The concept of surface fingerprint is proposed by generalizing the concept of human fingerprint to geographical space to identify the location of spatial objects. Surface fingerprint is the unique identification of a specific location on the earth. Similar to human fingerprint, it can be constructed with spatial feature points. If too many feature points are extracted from the image, the complexity of matching computation will greatly increase. In this paper, the spatial objects are used as the feature points and surface fingerprint can be constructed through the spatial relationship of these objects.

MIP of Geographical Location

"Machine intelligent perception of geographical location", also known as "machines automatically understanding the geographical location", means that the computer automatically obtains the feature points of the surface, constructs the surface fingerprint through a certain algorithm, and uses the surface fingerprint matching algorithm to automatically indicate the surface location. Obviously, the MIP of location is based on the concept of surface fingerprint. By constructing a large-scale surface fingerprint database, the machine can store the unique location identification at any location in the research area, so as to achieve the purpose of automatic and intelligent perception of location.

The Method of MIP of Urban Geographic Location

Automatic Extraction of Spatial Objects Based on Mask Region-Based Convolutional Neural Network (R-CNN)

Obviously, instance segmentation is the basis of machine perception of geographic location, which can effectively detect objects with relatively stable spatial morphological and spectral features. On high-resolution remote sensing images, playgrounds, crossroads, and bridges have stable spectral characteristics and morphology.

It is necessary to establish a training data set and test data set of instance segmentation model. For each picture in the data set, the position and shape of each object need to be marked in advance. For a playground, we directly mark the area enclosed by the runway edge. For a crossroad, we mark the area enclosed by the zebra crossing, and for a bridge, we mark the edge of the bridge area. Then it automatically calculates the bounding rectangle. Typical sample marks are shown in Figure 1. The yellow line in the figure is the outer boundary of the object of interest in the image.

There are 1200 images and 1330 labeled objects in the training sample data set, and 500 images and 589 labeled objects in the test data set. We selected three instance segmentation models, including TensorMask (Chen *et al.* 2019), CenterMask (Youngwan and Park 2020), and Mask Region-Based Convolutional Neural Network (R-CNN) to train the data sets, respectively. Stochastic gradient descent (SGD) is used to train these models. The test data set was used to extract and vectorize the spatial objects on each image, and the performance indexes of frames per second (FPS), mAP50, and mAP75 were counted, as shown in Table 1. It can be seen that Mask R-CNN has the best prediction accuracy in the three models. Therefore, we choose Mask R-CNN as the extraction model of spatial objects.

Table 1. Comparison of three models on test data set.

Model	Resolution	Backbone	FPS	mAP_{50} (%)	mAP_{75} (%)
TensorMask	512 × 512	ResNet-50-FPN	2.74	83.4	72.6
CenterMask	512 × 512	DLA_34	13.48	76.3	70.2
Mask R-CNN	512 × 512	ResNet-50-FPN	7.70	84.1	75.7

FPS = frames per second; R-CNN = Region-Based Convolutional Neural Network.

In order to improve the precision of the model and try to avoid the false detection, the category credibility thresholds of playground, crossroad, and bridge are set to 0.98, 0.98, and 0.97, respectively, with the higher overall precision and relatively high recall rate. The mask threshold is set to 0.5, the mask of spatial object extracted by Mask R-CNN is closest to the result of manual discrimination. Table 2 shows the training accuracy of test data set. The overall recall rate is 83.7% and the precision is 95.9%. Compared with the artificially marked mask, the average precision is 80.1%.

Figure 2 shows the extraction results of typical sample region. It can be seen from the figure that the extraction results of Mask R-CNN model are close to human interpretation, which meets the requirements of urban spatial object extraction.

However, although the model has relative high detection precision, under the influence of image blur, occlusion, and shadow, there are still some unrecognized objects. Figure 3 gives some undetected samples. Therefore, when the machine perceives the location, the error of automatic object extraction cannot be ignored, and its surface fingerprint construction and matching method must be fault-tolerant.

(a) (b) (c)

Figure 1. The typical spatial objects on high-resolution remote sensing images.

Table 2. The training accuracy of test data set with Mask R-CNN.

Object Type	Category Code	Number of Training Samples	Number of Test Samples	Category Credibility Threshold	Category Precision (%)		Mask Precision (%)
					Recall Rate	Precision	
Playground	1	437	198	0.98	84.8	96.6	83.5
Crossroad	2	450	206	0.98	83.0	96.1	75.3
Bridge	3	443	185	0.97	83.2	95.1	81.5
Total	—	1330	589	—	83.7	95.9	80.1

R-CNN = Region-Based Convolutional Neural Network.

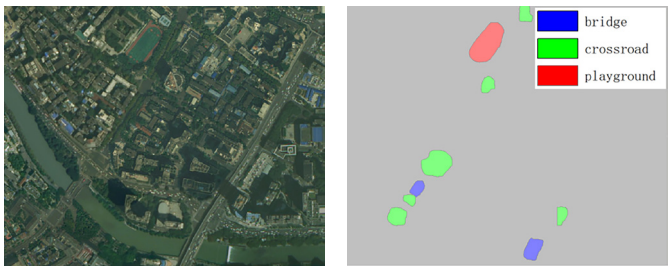

Figure 2. Typical result of object extraction from high-resolution remote sensing image.

Figure 3. Typical undetected spatial objects on high-resolution remote sensing images. (a) Playground; (b) crossroad; (c) bridge.

Spatial Object Coding and Automatic Construction of Urban Surface Fingerprint Database

Features of Spacial Object

Spatial object features include attribute features, location features, morphological features, and spatial relationship features, which are the keys of spatial object coding.

(1) Attribute features:

Mask R-CNN can extract not only the distribution range of the spatial objects, but also their category with high precision. Therefore, the category of the spatial objects is used as the attribute code.

(2) Location features:

The center position of a spatial object is used to measure its position. There are: the center of minimum bounding rectangle (the center of MBR), the geometrical center, the center of gravity, and so on. Transform the mask of each spatial object extracted by Mask R-CNN into vector polygon and then calculate the center position of the spatial object by its edge nodes.

(3) Morphological features:

There are many indexes to measure the spatial morphological features. Among the edge nodes of one spatial object, the connection between the farthest two nodes is called the major axis, and the length is expressed as d, as shown in Figure 4. The maximum distance from the node to the major axis is called the semi-minor axis, which is expressed as s. The oblateness of the spatial objects e is:

$$e = \frac{0.5d - s}{0.5d}. \tag{1}$$

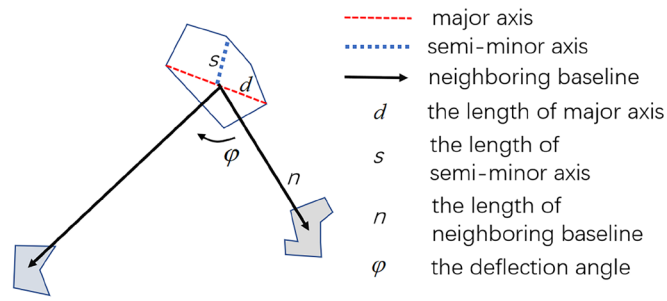

Figure 4. Typical morphological features and spatial relationship features of spacial object.

(4) Spatial relationship features:

The spatial relationship of spatial objects refers to the geometric relationship between each object and its neighboring objects, including the distance, orientation, and topology. Because the topological relationship is difficult to describe quantitatively, the relative distance and orientation between spatial objects are measured based on the neighboring baseline. Starting from the center of one spatial object, the ray connecting the center of its neighboring spatial object is called the neighboring baseline, and its rotation angle to the X axis is called the neighboring angle. The length of the line segment is called the neighboring distance, which is expressed as n. Figure 4 shows a schematic of the neighboring baseline and distance.

We take one of the neighboring objects as reference in order to measure other neighboring objects relatively. The angle difference between the neighboring baselines is called the deflection angle φ. The ratio of

their neighboring distances is called the neighboring distance coefficient ζ. Clearly, φ and ζ are all scale independent and rotation invariant.

Feature Selection for Spatial Object Coding

In order to ensure the availability and stability of surface fingerprint, it is necessary to select relatively stable spatial features that can be automatically extracted by computers for spatial object coding. In addition, the codes constructed by spatial features should be rotation invariant and scale independent so as to realize machine perception of geographical location.

(1) Data set preparation for feature selection:
In order to investigate the stability of different features, the city of Chengdu was chosen as the study area, and the playgrounds, crossroads, and bridges were extracted from the 18-level data of Google online satellite image and Tianditu online satellite image, respectively, to form their own object data set. There are 4329 objects and 4924 objects extracted from Google and Tianditu, respectively. We overlapped the two object data sets and marked the same two objects as an object pair with the same identifier. The number of object pairs is 2842, accounting for only 65.7% and 57.7% of their total number of objects, respectively.

(2) The best location measurement method of spatial object:
To select the best location measurement method, the object pairs with the following characteristics are selected, i.e., their nearest neighbor objects also belong to another object pair. These object pairs are used to calculate the neighboring distance and angle with different location measurement method. Table 3 shows the absolute errors of the two data sets. It can be seen from the table that with the location measurement method based on center of gravity, the average error of neighboring distance and neighboring angle is less than that of the other two methods. Therefore, the center of gravity is used to measure the location for each object.

Table 3. Neighboring distance and angle error of different location measurement methods.

Measurement Method	Neighboring Distance (m)		Neighboring Angle (°)	
	Average Error	Maximum Error	Average Error	Maximum Error
Center of MBR	4.53	39.5	1.2	22.6
Geometrical center	8.29	81.9	1.95	25.1
Center of gravity	4.06	39.8	1.14	22.4

MBR = minimum bounding rectangle.

(3) Comparison of stability between morphological characteristic parameters and spatial relationship characteristic parameters:
The major axis length, semi-minor axis length, and oblateness of each object pair are calculated, and then the parameter errors are compared with the nearest neighboring distance. Because the parameters have different units, the relative error s is used for the analysis:

$$\sigma = \frac{|\mu_1 - \mu_2|}{\mu_1}, \tag{2}$$

where μ_1 and μ_2 are the parameter value of the spatial objects extracted from Google and Tianditu, respectively.

The relative errors of morphological characteristic parameters are shown in Table 4. It can be seen that the relative errors of the major axis length, semi-minor axis length, and oblateness of the objects extracted from different remote sensing images are all larger than those of the nearest neighboring distance. It means that the spatial objects extracted by Mask R-CNN have lower stability of morphological features compared with the neighboring relationship. Spatial object coding should mainly consider the adjacency of the objects.

Table 4. Relative error of morphological characteristic parameters.

Oblateness		Semi-Minor Axis Length		Major Axis Length		Nearest Neighboring Distance	
Average Value	Peak Value	Average Value	Peak Value	Average Value	Peak Value	Average Value	Peak Value
3.186	8352	0.16	10	0.11	6.01	0.0032	0.72

Spatial Object Coding

Spatial object coding includes three parts: location coding, attribute coding, and spatial relationship coding.
(1) Location coding and attribute coding:
The coordinate of the gravity of the center of each object is regarded as its location code. Attribute coding uses landuse type code to represent the attributes of spatial objects. Table 2 gives the category codes of playgrounds, crossroads, and bridges.
(2) Spatial relationship coding:
A fixed-length string is used to store the spatial relationship codes. For each coded bit, the value range is limited to 0–35, 0–9 is coded as 0–9, and 10–35 are respectively coded with capital letters of A–Z.
For the central object to be coded, a certain number of nearest objects are searched. With one of the neighboring objects as reference, the other neighboring objects are coded according to the landuse type, distance, and angle in the order from near to far, forming a fixed length code, as shown in Figure 5.

In Figure 5, C_i is the neighboring object category code. D_0 and A_0 are distance code and angle code of the reference object. D_i and A_i ($i > 0$) are distance codes and angle codes of other neighboring objects. According to Figure 5, the length of the spatial relationship code is three times of N. D_0 and A_0 are coded with reference to major axis of the center object. To encode D_0, δ is calculated as follows:

$$\delta = \frac{n_0}{d}, \tag{3}$$

where n_0 is the neighboring distance of the reference object. δ will be rounded and clamped to 0–35 to get the code D_0.

To encode A_0, the angle between the major axis of the central object and the neighboring baseline of the reference object is calculated, divided by 10.

Based on the neighboring baseline of the reference object, D_i and A_i of other neighboring objects are coded. In order to expand the range of distance code as much as possible and enhance the robustness, Equation 4 is used to calculate the stretching value of distance coefficient:

$$r_i = \log_{1.15}\zeta, \tag{4}$$

where ζ is calculated as follows:

$$\zeta = \frac{n_i}{n_0} \quad (0 < i < N), \tag{5}$$

where n_i is the neighboring distance of the ith other nearest object. Based on the same coding method, the r_i in Equation 4 will be rounded and clamped to 0–35 to get the code D_i. Angle code A_i directly calculates the deflection angle φ of the neighboring baseline relative to the reference object, and converts it to 0–360, which then will be divided by 10 and rounded to get A_i.

Spatial relationship code actually demarcates the grades of angle and distance. The similar coding values correspond to a certain angle

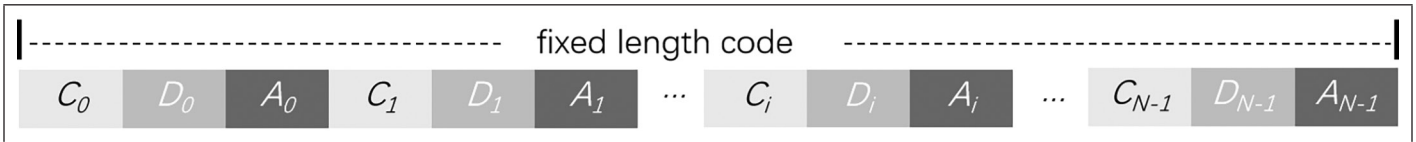

Figure 5. Spatial relationship coding.

or distance range, which ensures the robustness of machine perception algorithm of location to a certain extent.

(3) Selection of reference neighboring objects for spatial relationship coding:
For the same spatial object, choosing a different reference neighboring object will lead to different spatial relationship codes. Therefore, it is the premise of spatial object matching to select the same neighboring object for spatial relationship coding. In order to study the probability that different object data sets contain the same neighboring object, we still take the above-mentioned object pairs of Google and Tianditu as samples. For each pair, search m nearest objects in their own data set, and judge whether there is at least one same object. Count the number of object pairs which have the same neighbor under different *m* values, as shown in Figure 6.

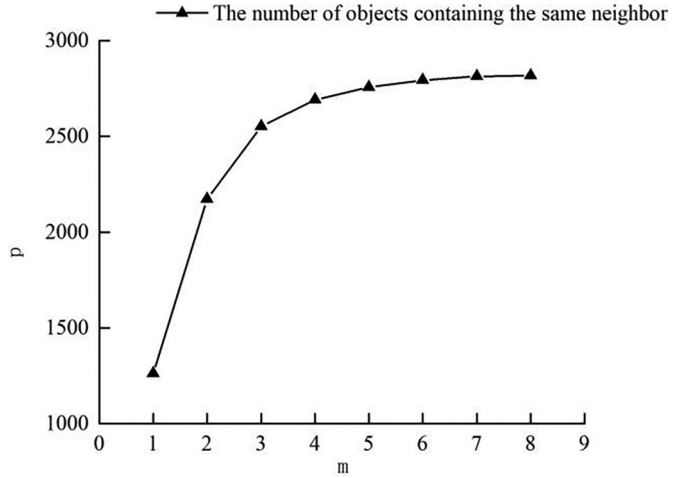

Figure 6. The number of objects with the same neighbor under different m values in the test area (*p* represents the number of object pairs which have the same neighbor, *m* represents the searched number of nearest neighbor objects).

It can be seen that when *m* takes 1, the number of object pairs which have the same nearest neighbor is 1261, only accounting for 25.6% and 29.1% of the total number of object pairs, respectively. When m takes 2, the value of *p* increases sharply, reaching 2173. Since then, the growth rate of *p* has been decreasing and the value of *p* approaching 2842.

Considering the matching rate and computational efficiency, the spatial relationship coding is constructed on the basis that m takes 2. For each spatial object, the nearest object and the next nearest object are used to construct its spatial relationship codes.

Establishment of Urban Surface Fingerprint Database

The spatial objects automatically extracted by computer are encoded and stored in the urban surface fingerprint database. For each of the spatial objects, the category code *C*, major axis *d*, projection coordinates, the spatial relationship code of the nearest object (FCode), and the next nearest object (SCode) are stored as a record, as shown in Table 5.

Table 5. Data table design of urban surface fingerprint database.

C	*d*	*X*	*Y*	FCode	SCode
1	91.22	11599...	3584...	2G021J23Q26627...	2DK20G22725N26...
…					

FCode = the spatial relationship code of the nearest object; SCode = the next nearest object.

MIP of Geographical Location

Technical Process of MIP of Geographic Location Based on Remote Sensing Image

Firstly, the spatial objects of regional remote sensing images are automatically detected by the Mask R-CNN model, and an urban surface fingerprint database is constructed. Then, the same Mask R-CNN model is used to detect and encode the spatial objects contained in a local remote sensing image.

Finally, the fingerprint matching algorithm is used to calculate geographic location of the spatial objects in local remote sensing image based on the urban surface fingerprint database. The technical flowchart is shown in Figure 7.

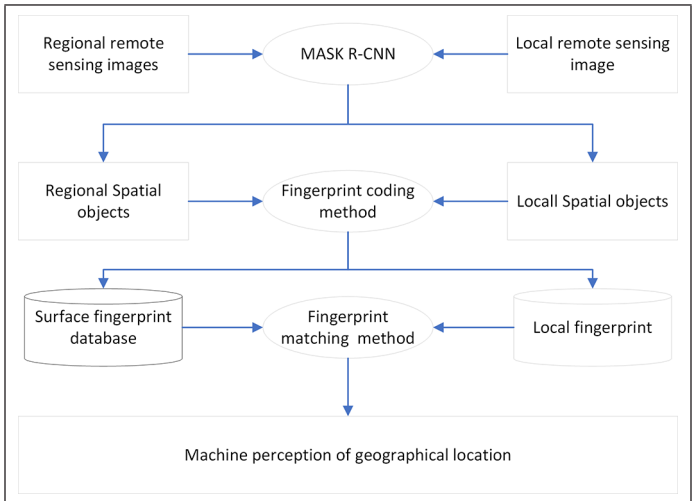

Figure 7. Technical flow of machine perception of geographical location based on remote sensing images.

Similarity Calculation of Spatial Object

(1) The similarity calculation algorithm:
It is assumed that a spatial object exists in both the fingerprint database and the local object set, and is represented as *S* and *L*, respectively. When using the spatial relationship codes to calculate the similarity between spatial objects *S* and *L*, their two codes match each other, and the maximum similarity among the four matches is taken as the similarity of *S* and *L*.

In each match in *S* and *L*, their codes are expressed as follows:

$$\begin{cases} F_S = \left\{ \left(C_i^S, D_i^S, A_i^S \right) \mid 0 \le i < N \right\} \\ F_L = \left\{ \left(C_i^L, D_i^L, A_i^L \right) \mid 0 \le i < N \right\} \end{cases}, \tag{6}$$

where F_S and F_L represent the code of *S* and *L*, and C_i, D_i, and A_i represent the category, distance, and angle codes of its neighboring objects, respectively. The equation for calculating the similarity of F_S and F_L is:

$$p_{SL} = \begin{cases} wp_1 & p_0 \ge a \\ 0 & p_0 < a \end{cases}, \tag{7}$$

where w is the matching coefficient, p_0 is the degree of the distance code matching of the reference object, p_1 is the average degree of code matching of other neighboring objects, and a is the similarity threshold. The equation to calculate p_0 is as follows:

$$p_0 = \begin{cases} 1 - \left(\left| D_0^S - D_0^L \right| \right) / 20 & \left(C_0^S = C_0^L \right) \\ 0 & \left(C_0^S \ne C_0^L \right) \end{cases}. \tag{8}$$

w and p_1 both involve the matching of other neighboring objects. Take out one of other neighboring objects from *S* and *L*, respectively, and their similarity is:

$$p_{ij} = \begin{cases} \left(1 - \left| D_i^S - D_j^L \right| / 5\right)\left(1 - \min\left(\left| A_i^S - A_j^L \right|, 36 - \left| A_i^S - A_j^L \right| \right) / 5\right) & \left(C_i^S = C_i^L \right) \cap \left(\left| D_i^S - D_j^L \right| < 2 \right) \\ 0 & \left(C_i^S \ne C_i^L \right) \cup \left(\left| D_i^S - D_j^L \right| \ge 2 \right) \end{cases}, \tag{9}$$

where i and j represent the order number of each neighboring object of S and L, respectively.

A certain neighboring object in L traverses all other neighboring objects in S in turn, and the similarity is calculated according to Equation 9. If the maximum similarity is greater than or equal to α, it is considered that the neighboring object has found a match among the neighboring objects of S. Then, p_1 is calculated by Equation 10:

$$p_1 = \frac{1}{N_{SL}} \sum_{j=1}^{N_{SL}} p_{ij}, \tag{10}$$

where N_{SL} is the matching number of other neighboring objects. The matching coefficient w can be calculated by:

$$w = \begin{cases} 0.1\dfrac{N_{SL} - \beta}{N - \beta} + 0.9 & N_{SL} >= \beta \\ 0 & N_{SL} < \beta \end{cases}, \tag{11}$$

where β is the minimum matching number of neighboring objects required for spatial object matching.

For each of objects in the local object set, traverses all objects in the fingerprint database to find the object with the maximum similarity. If the maximum similarity is greater than or equal to the similarity threshold α, take the object as the matching one.

(2) Determination of the number of nearest objects participating in coding: In order to obtain the best number of nearest objects participating in encoding, each object in Google data set and Tianditu data set is encoded. We set $\alpha = 0.75$ (which will be proved to be the best parameter later), increased β from 7 to 10, traversed the code of each object in the Tianditu data set, and searched for the matching object with the highest similarity from the Google data set. If they have the same identifier, the correct match is considered to be found. The number of correct matches is calculated, as shown in Table 6.

It can be seen from the table that when β is fixed, with the increase of N, the number of correct matches first increases and then remains stable or even decreases slightly. This means that in order to find the matched object from database, a certain number of nearest objects are required to construct a spatial relationship code. Because the objects extracted by Mask R-CNN are unreliable, too many nearest objects may have a negative impact on matching to a certain extent. Therefore, it is necessary to find a reasonable number of nearest objects participating in coding. As can be seen from the table, the peak value of N is related to β, which is about 2.4 to 2.7 times the value of β.

On the other hand, it is necessary to set a fixed length for spatial relationship code in the fingerprint database. Considering that in the actual matching, the larger the value of β, the higher the requirements for the number of objects extracted from the local remote sensing image, β is set to about 7–10, so N is set to 24 to encode spatial relationship with a length of 72. During the matching calculation, refer to Table 6 to obtain the best number of nearest objects from the spatial relationship code for calculation.

(3) Study on the optimal value of α and β:
To get the optimal value of α and β, we also count the total matches P_t and correct matches P_r under different values of α and β, as shown in Figure 8.

As can be seen from the figure, when β is fixed, with the increase of a, P_t deceases and P_r increases first and then decreases, reaching a peak near 0.75. It shows that the optimal parameter of a is 0.75. Figure 8d shows the values of P_t and P_r under different conditions of β when $\alpha = 0.75$. It can be seen that with the increase of β, P_t is constantly decreasing while P_r increases first and then decreases, and reaches the optimum at 11.

Fingerprint Matching Algorithm

It can be seen from Figure 8, it is difficult to ensure that the object with maximum similarity is the correct one only considering the similarity of spatial relationship codes. Further filter is required. If there are two objects L_1 and S_1, L_1 is from the local object data set, S_1 is from the fingerprint database which matches L_1. The nearest N objects of L_1 and S_1 are searched respectively. If the number of neighboring objects is less than N, the actual number is used. Each of the neighboring objects of L_1 is represented as L_2. The best similar object of L_2, which is named as S_2, is searched from the neighboring objects of S_1. If S_2 is found, the rotation, skewing and scaling factors from the coordinate system of the local image to the coordinate system of the finger database are calculated by using the four objects, including L_1, L_2, S_1, and S_2. According to Equation 12, the factors are used to verify the matching effectiveness of spatial relationship code firstly.

Table 6. Correct matches with different number of nearest objects participating in coding.

	Correct Matches			
N	***b* = 7**	***b* = 8**	***b* = 9**	***b* = 10**
14	1579	1281	871	448
18	1783	1810	1723	1513
19	1795	1832	1825	1768
20	1767	1839	1846	1779
21	1745	1821	1866	1854
22	1730	1817	1886	1890
23	1726	1804	1866	1905
24	1715	1799	1854	1907
25	1703	1785	1847	1897
28	1702	1781	1830	1877
60	1679	1715	1751	1778

$$|zd^L - d^S| \le \varepsilon, \tag{12}$$

where z is the scaling factor, d^L and d^S are the major axis of the local object and the object in the fingerprint database, respectively, and ε is the distance threshold.

If the relationship between scaling factor and major axis satisfies Equation 12, the neighboring objects of L_1 are traversed and their real coordinates are calculated according to the rotation, skewing, and scaling factors. Within a distance of ε, the matched object for each of the neighboring objects of L_1 is searched from the neighboring objects of S_1 by their real coordinates. If the number of matches is equal to or bigger than 3, the fingerprint matching is considered successful.

Table 7 shows the accuracy of fingerprint matching under different values of ε when α is assigned to 0.75 and β is assigned to 7.

As can be seen from Table 7, ε is related to the spatial scale of the extracted object. With the increase of ε, both the number of total matches and the correct matches increase, but the correct rate decreases. If the correct rate is required to be at least 95%, the optimal value in the experimental data is about 50 m.

In order to study the improvement of the accuracy of fingerprint matching, α and ε are set to 0.75 and 50, respectively, and accuracy rate is compared to that of similarity matching of spatial relation code with different β values, as shown in Table 8. It can be seen from Table 8 that based on the similarity calculation of spatial relationship code, the matching results are further filtered by using fingerprint matching algorithm, and the filtered objects has more than 95% probability of being the correct matched object.

Fingerprint matching algorithm is the bedrock of machine perception for geographical location. In the local object set, as long as there is

Table 7. Matching accuracy of fingerprint matching under different values of ε.

ε (m)	Total Matches	Correct Matches	Correct Rate (%)
10	1413	1408	99.6
25	1619	1589	98.1
50	1746	1667	95.5
75	1867	1711	91.6
100	1976	1726	87.3
125	2099	1744	83.1
150	2443	1762	72.1

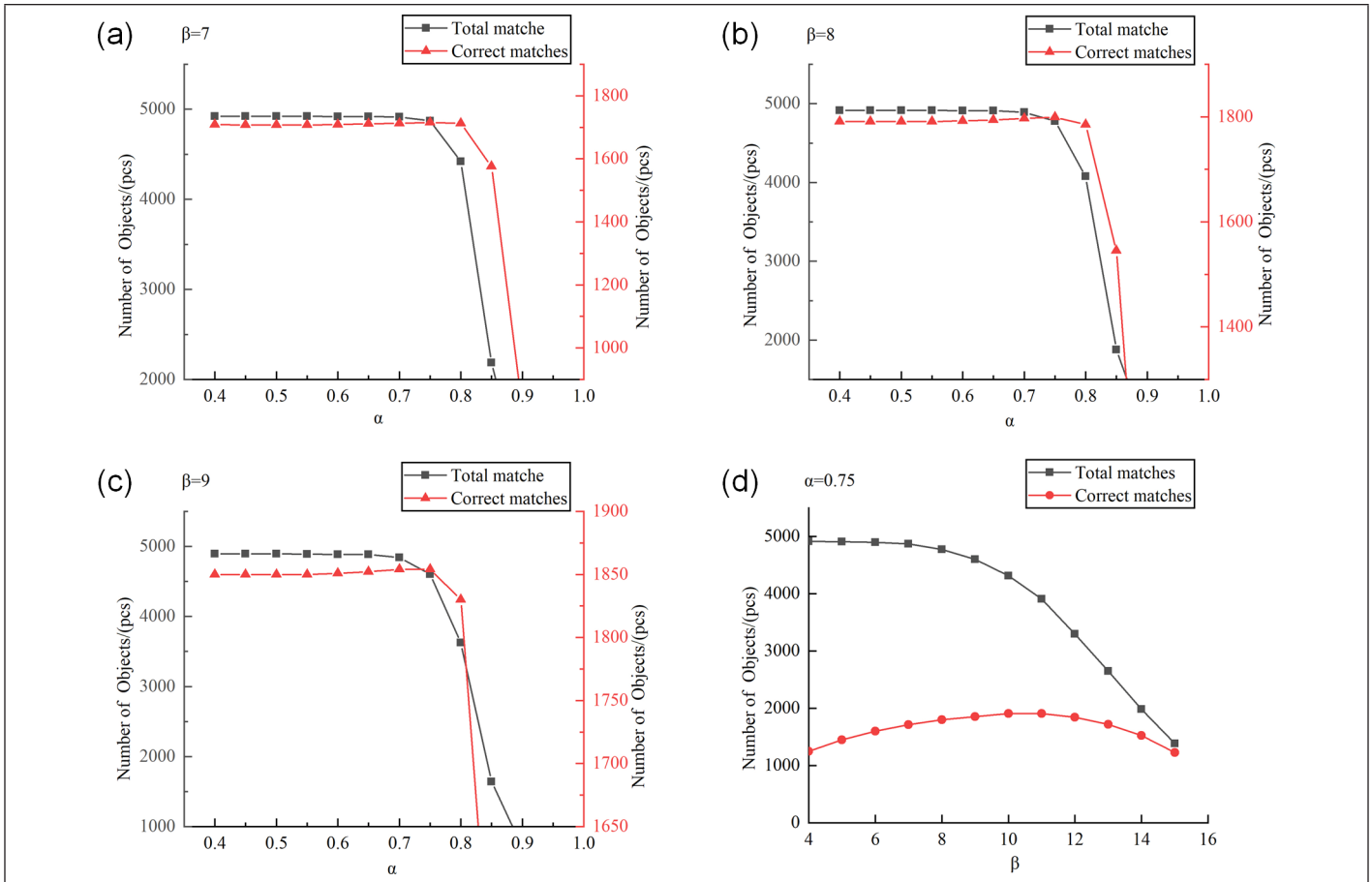

Figure 8. Parameter analysis of similarity calculation of spatial objects. (a) Total number of matches and correct number of matches when $\beta = 7$. (b) Total number of matches and correct number of matches when $\beta = 8$. (c) Total number of matches and correct number of matches when $\beta = 9$. (d) Total matching number and correct matching number when $\alpha = 0.75$. pcs = pieces.

one object whose matched object is founded from fingerprint database, we can use the matched object in the fingerprint database and its adjacent matched objects to automatically perceive the geographical location of the local remote sensing image.

Performance Evaluation of Fingerprint Matching Algorithm

In Table 8, we also calculated average matching time required for each object. The CPU of the experimental computer is an Intel® core (TIM) i7-7700. The matching time of a single local object is directly proportional to the number of records in the fingerprint database. The number of objects searched in the Google data set in the experiment is 4329, and the matching time is about 0.012s when β is equal to 7. According to this, when the number of spatial objects in the fingerprint database is less than about 360 000, the matching time of a single object will not exceed 1 s.

Experiments and Results

Establishment of Experimental Fingerprint Database in Major Cities of China

Taking major cities in China as examples, 18-level Google online satellite image were used to extract playgrounds, crossroads, and bridges. Due to the irregularity of urban area, we only extracted spatial objects in the main urban area. For example, we only extracted the central area of Wuhan. As for Hangzhou, we only chose the urban area near Qiantang River. A total of 13 649 spatial objects were extracted, as shown in Table 9. The code of each spatial object was stored in the fingerprint database.

Table 9. Experimental fingerprint database of major cities in China.

City	Playground	Crossroad	Bridge	Total	Area (km^2)	Density (per km^2)
Fuzhou	276	1624	628	2528	710.41	3.55
Hangzhou	153	849	348	1350	306.33	4.41
Nanjing	606	1890	525	3021	740.21	4.08
Wuhan	475	1636	720	2831	776.86	3.64
Changsha	179	879	208	1266	270.58	4.68
Guangzhou	349	1299	1005	2653	679.33	3.91
Total	2038	8177	3434	13649	3483.72	3.92

Table 8. The accuracy rate and average matching time of each object of fingerprint matching compared to that of similarity matching of spatial relation code.

	Similarity Matching of Spatial Relation Code				Fingerprint Matching			
β	Total Matches	Correct Matches	Accuracy Rate (%)	Average Time (s)	Total Matches	Correct Matches	Accuracy Rate (%)	Average Time (s)
7	4661	1795	38.5	0.012	1746	1667	95.5	0.012
8	4449	1839	41.3	0.012	1765	1704	96.5	0.013
9	4359	1886	43.3	0.014	1803	1736	96.3	0.015
10	4316	1907	44.2	0.016	1829	1763	96.4	0.017

The Experiment of MIP of Urban Geographic Location

To prove the performance of the proposed method, we cut 200 local remote sensing images from Tianditu in different areas of the cities listed in Table 9.

We have ensured that the number of objects contained in each local image is greater than or equal to 7. In this experiment, the number of successful matches was 184 and the number of failures was 16, with a matching rate of 92%. Figure 9 shows two typical cases of MIP of geographical location. Figure 9a and 9d visualize two local areas of the urban surface fingerprint database. Figure 9b and 9e show local objects of two local areas extracted from local remote sensing images based on Tianditu online satellite images. Figure 9c and 9f show the fingerprint matching results in two cases. The first case shown in the first row contains all types of objects extracted, such as playground, crossroad, and bridge, of which 12 of the 17 objects are successfully matched. The second case shown in the second row contains only the extracted crossroads, of which eight of the nine objects are successfully matched.

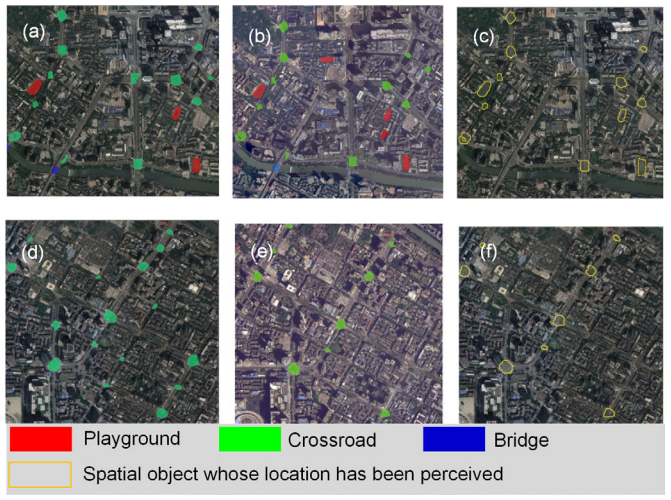

Figure 9. Two typical cases of MIP of geographical location. Local visualization (a) and (d) of urban surface fingerprint database for extracted objects from different areas of Google online satellite images. Local objects (b) and (e) extracted from the two areas of local remote sensing images (based on Tianditu online satellite images). Location perception results (c) and (f) of the two areas.

Method Adaptability Analysis

We tried to scale and distort local images to test the performance of machine geographical location perception under different conditions. In Figure 10a, we rotated the original local image by 12° and reduced the resolution from 0.597 m to 0.70 m. Figure 10b shows the location perception results. This proves the angle independence and scale independence of fingerprint matching.

In Figure 10c, we distorted the origin local image as shown in Figure 9b to a certain extent. Most of the perceived objects in Figure 10d are the same as those in Figure 9c. This proves that the fingerprint matching has a certain degree of robustness. Compared with Figure 9c, the imperceptible objects mainly come from areas where the degree of distortion exceeds the matching parameter ε of Equation 12, or the local deformation exceeds the recognition ability of the model.

Although the fingerprint matching algorithm is scale independent, the object extracted by Mask R-CNN is closely related to the spatial scale. In order to test the sensitivity of the image resolution, we resampled the local image shown in Figure 9b according to the multiples of 0.25, 0.5, 0.7, 1.2, 1.5, and 2.0, respectively. The objects extracted by Mask R-CNN are shown in Figure 11a– f.

It can be seen from the figure that the Mask R-CNN model has a most suitable resolution range. In this example, except for the resolution of 0.150 m and 1.194 m, the objects extracted from other images can be used to complete machine location perception successfully, which reflects that the spatial scale of this method has a certain degree of

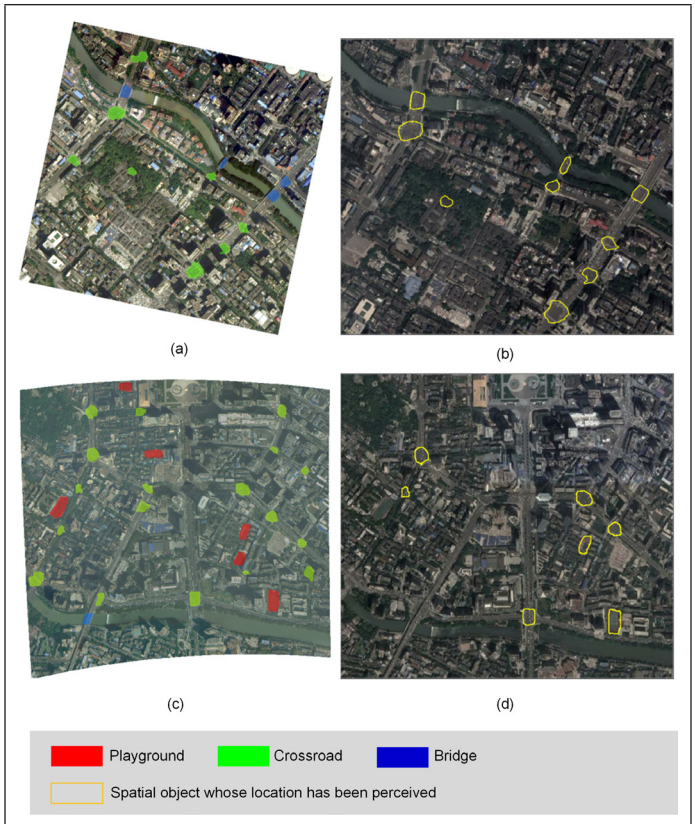

Figure 10. A typical case of MIP of geographical location. (a) The extraction result of rotated and reduced local image. (c) The extraction result of distorted local image. (b) and (d) result of location perception of locations.

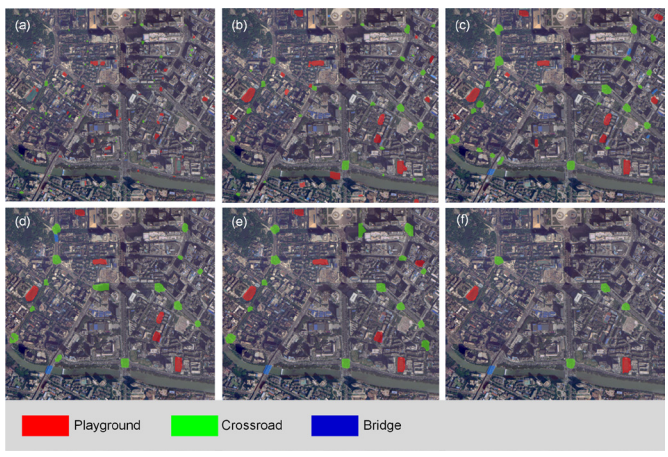

Figure 11. Object extraction result of the resampled local image with different resolutions.

robustness to a certain extent. However, if the resolution is too small or too large, such as 0.150 m and 1.194 m in this example, the spatial scale of the image exceeds the best suitable range of Mask R-CNN model, resulting in huge differences between the local fingerprint and the fingerprint database and unable to complete machine location perception.

Discussion

Through the above experiments, we find that the method of location intelligent perception has high accuracy for urban high-resolution images, and has angle independence, certain robustness, and spatial scale independence. Because this method is based on Mask R-CNN to extract spatial objects, the ability of machine location perception is limited by this model. In order to further improve the machine's ability to precept the location, there are several potential problems should be considered.

The first problem is the distribution density of extracted objects. As shown in Table 9, the density of extracted objects is greater than 3.5 per km^2, which means that if the coverage area of the local urban image is more than 2 km^2, the number of objects may exceed 7, and computers will be able to find the position automatically. However, there are some errors in the object extraction by Mask R-CNN, the minimum area requirement of local image for machine perception position may be greater than 2 km^2, which depends on the quality of the local image and the number of objects contained.

The second problem is the similarity of object distribution between the local image and fingerprint database. If there are great differences in imaging time and image quality between the local image and the image used in the establishment of fingerprint database, the number of effective spatial objects extracted from the remote sensing image will be insufficient to realize location perception. It is necessary to update the fingerprint database at any time.

The third challenge is the consistency between the spatial scale of local image and that of fingerprint database. Although Mask R-CNN has certain spatial scale robustness, it still has a suitable spatial scale range. To correctly perceive the location, the spatial scale of local image and fingerprint database must be similar.

It is noted that the key parameters are based on the data of the experimental area, which may deviate from the ideal parameters.

Conclusion

A preliminary study on MIP of geographical location based on high-resolution remote sensing images is carried out. First, the surface fingerprint is defined as the unique identification of the surface. In order to achieve MIP of geographical location, the instance segmentation model Mask-RCNN is introduced, and a relatively reliable model of extracting spatial object is automatically obtained through sample training. Then, the position, attribute, morphological, and spatial relationship features of the spatial objects are analyzed. It is found that the gravity center is superior to other location measurement, and the neighboring relationship features of the spatial object are more stable than the morphological features. Therefore, a location measurement method for spatial objects based on gravity center and a spatial relationship measurement method based on neighboring baseline are proposed. The surface fingerprint database is constructed by encoding the spatial relationship of 24 nearest objects for each of the spatial objects. Through the spatial object coding similarity algorithm and fingerprint matching algorithm, the technical route of MIP of geographic location based on remote sensing images is formed.

Finally, through the experiments of geographical location machine perception in major cities of China, the feasibility of this method is proved, which provides a new method for the in-depth study of geographical location MIP. In future work, we will enrich the diversity of spatial object categories, and build fingerprint databases with multiple spatial scales to further improve the accuracy of MIP.

Acknowledgment

This project is funded by National key R&D plan (2018YFB0505300) and science and technology projects of SiChuan Province (2020YFG0146).

References

Abrams, M. 2017. Global geoscience maps from ASTER data. Pages 4477–4478 in *Proceedings IEEE International Geoscience and Remote Sensing Symposium*. https://doi.org/10.1109/IGARSS.2017.8127994.

Bay, H., T. Tuytelaars and L. V. Gool. 2006. SURF: Speeded up robust features. Pages 404–417 in *Proceedings of the 9th European Conference on Computer Vision—Volume Part I*, held in Graz, Austria, 7–13 May 2006. Edited by A. Leonardis, H. Bischof and A. Pinz. Berlin: Springer-Verlag.

Chen, M., Z. Shao, C. Liu and J. Liu. 2013. Scale and rotation robust line-based matching for high resolution images. *Optik—International Journal for Light and Electron Optics* 124(22):5318–5322.

Chen, X., R. Girshick, K. He and P. Dollar. 2019. TensorMask: A foundation for dense object segmentation. Pages 2061–2069 in *Proceedings 2019 IEEE/CVF International Conference on Computer Vision (ICCV)*. https://doi.org/10.1109/ICCV.2019.00215.

Fan, Z. and Q. Zhao. 2012. A data-clustering based robust SIFT feature matching method. *Journal of Computer Research and Development* 49(5):1123–1129.

He, K., G. Gkioxari, P. Dollár and R. Girshick. 2017. Mask R-CNN. *IEEE Transactions on Pattern Analysis and Machine Intelligence* 42(2): 386–397.

Hewson, R. and D. Robson. 2014. Evaluating the information content of National ASTER geoscience maps in the Wagga Wagga and Cobar regions of New South Wales. *Preview*:45–49.

Jiang, X., J. Ma, G. Xiao, Z. Shao, X. Guo. 2021. A review of multimodal image matching: Methods and applications. *Information Fusion* 11(2021):22–71.

Kovacs, A. and T. Sziranyi. 2013. Improved Harris feature point set for orientation-sensitive urban-area detection in aerial images. *IEEE Geoscience and Remote Sensing Letters* 10(4):796–800.

Lee, Y. and Park, J. 2020. CenterMask: Real-time anchor-free instance segmentation. Pages 13903–13912 in *Proceedings 2020 IEEE/CVF Conference on Computer Vision and Pattern Recognition (CVPR)*, held in Seattle, Wash., 13–19 June 2020.

Liu, Z., J. An and J. Yu. 2012. A simple and robust feature point matching algorithm based on restricted spatial order constraints for aerial image registration. *IEEE Transactions on Geoscience and Remote Sensing* 50(2):514–527.

Matsuoka, M. and S. Midorikawa. 1993. Prediction of isoseismal map for large area using the digital national land information. *Journal of Structural and Construction Engineering* 447:51–56.

Moosavi, V. 2017. Contextual mapping: Visualization of high-dimensional spatial patterns in a single geo-map. *Computers, Environment and Urban Systems* 61(Part A):1–12.

Rublee, E., V. Rabaud, K. Konolige and G. Bradski. 2011. ORB: An efficient alternative to SIFT or SURF. Pages 2564–2571 in *Proceedings IEEE International Conference on Computer Vision*, held in Barcelona, Spain, 6–13 November 2011. https://doi.org/10.1109/ICCV.2011.6126544.

Rucheng, L. U., H. Xianjin, Z. Tianhui, X. Sisi, Z. Xingyu and Z. Xiaofeng. 2009. Construction of land use information Tupu in the rapidly developing regions: A case study of the surrounding regions of Taihu Lake in Jiangsu Province. *Resources Science*:49–57.

Su, J., Q. Xu and J. Zhu. 2010. A scene matching algorithm based on SURF feature. Pages 434–437 in *Proceedings IEEE International Conference on Image Analysis and Signal Processing*, held in Xiamen, China. https://doi.org/10.1109/IASP.2010.5476080.

Tong, J., J. Yu, C. Wu and G. Yu. 2021. Health information acquisition and position calculation of plug seedling in greenhouse seedling bed. *Computers and Electronics in Agriculture* 185(3):106146.

Vishwakarma, A. and M. K. Bhuyan. 2020. Image mosaicking using improved auto-sorting algorithm and local difference-based Harris features. *Multimedia Tools and Applications* 79(1):23599–23616.

Wang, X. G., F. C. Wu and Z. H. Wang. 2008. Harris feature vector descriptor (HFVD). Pages 1–4 in *Proceedings IEEE International Conference on Pattern Recognition*. https://doi.org/10.1109/ICPR.2008.4760977.

Wu, Y. 2019. Research on feature point extraction and matching machine learning method based on light field imaging. *Neural Computing and Applications*:8157–8169.

Yang, H., X. Li, L. Zhao and S. Chen. 2019. A novel coarse-to-fine scheme for remote sensing image registration based on SIFT and phase correlation. *Remote Sensing* 11(15):1833.

Yao, L., H. Feng, Y. Zhu, Z. Jiang, D. Zhao and W. Feng. 2009. An architecture of optimised SIFT feature detection for an FPGA implementation of an image matcher. Pages 30–37 in *Proceedings IEEE International Conference on Field-Programmable Technology*. https://doi.org/10.1109/FPT.2009.5377651.

Zhou, H., Y. Yuan and C. Shi. 2009. Object tracking using SIFT features and mean shift. *Computer Vision and Image Understanding* 113(3):345–352.

IN-PRESS ARTICLES

Gaofei Yin. Smartphone Digital Photography for Fractional Vegetation Cover Estimation.

Xuzhe Duan, Qingwu Hu, Pengcheng Zhao, and Shaohua Wang. A low-cost and portable indoor 3D mapping approach using biaxial line laser scanners and a one-dimension laser rangefinder integrated with MEMS.

Toshihiro Sakamoto, Daisuke Ogawa, Satoko Hiura, Nobusuke Iwasaki. Alternative procedure to improve the positioning accuracy of orthomosaic images acquired with Agisoft Metashape and DJI P4 Multispectral for crop growth observation

Guangyun Li, Senzhen Sun, Yangjun Gao, Li Wang. Robust Dynamic Indoor Visible Light Positioning Method Based on CMOS Image Sensor.

Zhenfeng Shao, Hongping Zhang, Wenfu Wu, Xiao Huang, Jisong Sun, Jinqi Zhao, Yewen Fan. Comparing the sensitivity of pixel-based and sub-watershed-based AHP to weighting criteria for flood hazard estimation.

Gang Qiao, Hongwei Li. Lake Water Footprint Determination Using Linear Clustering-based Algorithm and Lake Water Changes in the Tibetan Plateau from 2002 to 2020.

Jason Parent, Chandi Witharana, Michael Bradley. Classifying and georeferencing indoor point clouds with ARCGIS.

Paul Pope, Brandon Crawford, Anita Lavadie-Bulnes, Emily Schultz-Fellenz, Damien Milazzo, Kurt Solander, Carl Talsma. Towards Automated/Semi-Automated Extraction of Faults from Lidar Data

Li Tan, Guoming Li, Xin Liu, Aike Kan. Feature-based convolutional neural network for very-high-resolution urban imagery classification

Ravi Dwivedi, Syed Azeemuddin. Conjunctive use of Landsat-8 OLI and MODIS Data for Delineation of Burned Areas

Chih-Hung Hsu, Che-Hao Chang, Chih-Tsung Hsu, Shiang-Jen Wu, Po-Hsien Chung. Hydrological Topography Dataset (HTD) - the Dataset for High Resolution 2D Urban Flood Modeling.

Xiaojun Yang, Feilin Lai. Improving land cover classification over a large coastal city through stacked generalization with filtered training samples.

Xiaoyue Wang, Hongxin Zhang, Dailiang Peng. Evaluation of urban vegetation phenology using 250 m MODIS vegetation indices.

Zhihua Xu, Xingzheng Lu, Wenliang Wang, Ershuai Xu, Rongjun Qin, Yiru Niu, Xu Qiao, Feng Yang, Rui Yan. Monocular Video Frame Optimization through Feature-based Parallax Analysis for 3D Pipe Reconstruction.

Lin Ding, Hanchao Zhang, Deren Li, Monitoring and Analysis of Urban Sprawl based on Road Network Data and High-resolution Remote Sensing Imagery: A Case Study of China's Provincial Capitals.

Xueyan Li, Heqing Zhang, Zhenxin Wang, Junfeng Song. Transformer for the Building Segmentation of Urban Remote Sensing.

Identifying the Driving Factors of Urban Land Surface Temperature

Lifeng Liang, Benhua Tan, Sicheng Li, Zhiming Kang, Xiujuan Liu, and Lihua Wang

Abstract

*Land surface temperature (*LST*) has a profound impact on urban climate and ecology, and is widely used to quantify surface urban heat islands. The spatial heterogeneity of* LST *is affected by natural and human factors, with seasonal differences. This study selected Dongguan, a rapidly urbanizing city in China, as an example to analyze the relationship between the spatial heterogeneity of* LST *in different seasons and influencing factors in six dimensions. Multi-source spatial data were combined, including Landsat images, meteorological data, digital elevation models, National Polar-Orbiting Partnership Visible Infrared Imaging Radiometer Suite nighttime light, and points of interest. The results show that spatial patterns of* LST *across different seasons were consistent, although there were local differences. Based on the GeoDetector model, the result indicated differences between separate effects and interactive effects, and identified the high temperature risk areas.*

Introduction

Land surface temperature (LST) is a key parameter affecting the balance of land surface radiation, climate, and environmental changes (K. Wang and Liang 2009). During rapid urbanization, the extent to which human activities affect and transform the land surface increases. The natural land surface is replaced by an artificial surface, which causes the urban land surface temperature to be significantly higher than the suburban land surface temperature, and surface urban heat islands (SUHIs) have become a global urban environmental problem, with a profound impact on health, energy consumption, economic development, and biological phenology (Faroughi *et al.* 2020; Y. Li *et al.* 2020; Mirzaei *et al.* 2020; X. Li *et al.* 2021).

LST inversion is the premise underpinning the quantitative analysis of the spatial heterogeneity of LST; the commonly used methods are mainly divided into two categories. The first method uses meteorological data recorded by ground stations, combined with mathematical statistics, to analyze temperature differences between urban and suburban areas, then analyzes the characteristics of spatial differences in LST (Eludoyin *et al.* 2014). The second method is a quantitative inversion of the LST based on thermal infrared remote sensing data. Compared with observed data from traditional ground meteorological stations, the latter offer wide coverage and high resolution, providing support for research on LST in widespread areas (Liu *et al.* 2021). Currently, Moderate Resolution Imaging Spectroradiometer (MODIS), Landsat, and Advanced Very High Resolution Radiometer (AVHRR) satellite data are widely used to evaluate the spatial distribution of LST (Balling and Brazel 1998; T. Liu *et al.* 2015; Zhao *et al.* 2021). The radiation transfer equation method proposed by Sobrino is based on the Landsat Thematic Mapper 5 with high accuracy (Sobrino *et al.* 2004; Y. Wang *et al.* 2021).

Research on the spatial heterogeneity of LST is essential for analyzing the formation and evolution of SUHIs, which can also can help improve the quality of life for residents, enhance the health of urban ecology, and provide pertinent information for the formulation of sustainable development strategies (Zhou *et al.* 2017). Analysis of the spatial heterogeneity of LST comprises two key decision points: the selection of driving factors and the selection of the analysis method. For the first decision, most researchers tend to select a single factor and ignore the influence of comprehensive factors such as meteorology, landscape pattern, and social development. Liu *et al.* (2021) analyzed the impact of land cover types on the spatial patterns of LST in Tokyo from 2001 to 2015; Baldinelli and Bonafoni (2015) suggested that albedo was the dominant factor affecting the spatial variability of LST in Florence, Italy; and Huang *et al.* (2016) compared MOD11A2 surface temperature data with Defense Meteorological Satellite Program Operational Linescan System nighttime light remote sensing data and analyzed the impact of socioeconomic activities on the spatial differentiation of LST. Hua *et al.* (2020) analyzed the relationship between SUHIs, impervious surface, and vegetation coverage in Xiamen, China, and concluded that the coverage of impervious surface is closely related to changes in SUHIs.

For the second decision, previous studies have mainly identified the dominant factors using traditional mathematical statistical methods, such as geographically weighted regression, ordinary least-squares regression analysis, or Pearson correlation analysis. However, these methods neglect the influence of interactions between different influencing factors on LST, which makes it difficult to carry out in-depth research on the spatial heterogeneity of LST or SUHIs (Chen *et al.* 2017). J. F. Wang and Hu (2012) proposed the GeoDetector model, which is a geospatial statistical method that can be used to analyze the spatial heterogeneity of geographical phenomena and reflects underpinning drivers. This method does not need to consider the collinearity of independent variables, and has been applied to quantify the impact of potential driving factors on geographic phenomena (Zhu *et al.* 2020).

Dongguan city was selected as the research area. Remote sensing data, digital elevation models, points of interest, and other spatial data served as the data sources, which were combined with the GeoDetector model to compensate for two shortcomings identified in the literature and designed to address two research questions:

(1) How do natural and human factors such as topography, meteorology, vegetation, water bodies, socioeconomics, surface reconstruction intensity, and landscape patterns affect the spatial heterogeneity of LST?
(2) How do the interactive effects of the driving factors influencing the spatial heterogeneity of LST differ from the separate effects?

Lifeng Liang, Sicheng Li, Zhiming Kang, and Xiujuan Liu are with the School of Geographical Sciences, Lingnan Normal University, Zhanjiang, 524048, China (Xiujuan Liu: 544022065@qq.com).

Benhua Tan is with the Department of Geography and Spatial Information Techniques, Ningbo University, Ningbo, 315211, China.

Lihua Wang is with the Department of Geography and Spatial Information Techniques, Collaborative Innovation Center for Land and Marine Spatial Utilization and Governance Research, Ningbo University, Ningbo, 315211, China (wanglihua1@nbu.edu.cn).

Contributed by Zhenfeng Shao, July 15, 2021 (sent for review October 29, 2021; reviewed by Nan Yang, Hongping Zhang).

Photogrammetric Engineering & Remote Sensing
Vol. 88, No. 4, April 2022, pp. 233–242.
0099-1112/22/233–242

doi: 10.14358/PERS.21-00043R3

Urban Land Cover/Use Mapping and Change Detection Analysis Using Multi-Temporal Landsat OLI with Lidar-DEM and Derived TPI

Clement E. Akumu and Sam Dennis

Abstract

The mapping and change detection of land cover and land use are essential for urban management. The aim of this study was to map and monitor the spatial and temporal change in urban land cover and land use in Davidson County, Tennessee in the periods of 2013, 2016, and 2020. The urban land cover and land use categories were classified and mapped using Random Forest algorithm. A combination of Landsat Operational Land Imager (OLI) satellite data with Light Detection and Ranging (lidar)-Digital Elevation Model (DEM) and derived Topographic Position Index (TPI) were used in the classification and monitoring of urban land cover and land use change. The urban land cover and land use types were mapped with average overall accuracies of about 87% in 2020, 85% in 2016 and 2013. The overall accuracy increased by around 8%, 9%, and 6% in 2020, 2016, and 2013 classifications respectively when lidar-DEM and derived TPI were added to Landsat OLI satellite data in the classification relative to standalone Landsat OLI. Total change occurred in about 63% of Davidson County between 2016 and 2020 with significant net gains and losses among land cover and land use types. This information could support land use planning.

Introduction

Land cover change is defined in this study as any change in the land biophysical characteristics including but not limited to vegetation and soil properties, whereas land use change is associated with the alteration of land by humans. Urban land use change is generally driven by urban growth, and this can lead to loss of natural vegetation and open space, a decline in connectivity of wetlands and wildlife habitats, and a loss in biodiversity (Patel et al. 2019; Verma et al. 2020). The understanding of urban land cover and land use change can provide insights on the impacts of land management practices and feedback to the environment to better manage land resources. Furthermore, it helps to quantitatively project future change in urban land cover to support land use management and planning. A change in land cover and land use category alters land biophysical surface characteristics and this can lead to significant consequences including but not limited to land degradation, water pollution, expedition of climate change, and changes to ecosystem services (Foley et al. 2005; Homer et al. 2020; Pielke 2005).

The Davidson County constitutes the largest city of Nashville in Tennessee and has experienced significant growth in population over the years with a population of around 477 800 in 1980 to approximately 678 889 in 2015 (Mojica 2018; United States Census Bureau 2018). The population growth in Davidson County is expected to influence land cover and land use change. Therefore, there is a need to spatially and explicitly detect and monitor the land cover and land use change in Davidson County to support urban planning and management. The use of multi-source and temporal data such as Landsat Operational Land Imager (OLI) in combination with Light Detection and Ranging (lidar)-Digital Elevation Model (DEM) and derived Topographic Position Index (TPI) could improve the detection, monitoring and change detection analysis of urban land cover and land use classification. This is because land cover and land use types respond to electromagnetic radiation differently and their spectral information is useful to map and monitor spatial and temporal change in land cover categories. A TPI is simply the difference between a cell elevation value and the average elevation of the neighborhood around that cell (Weiss 2001). The positive values of TPI mean the cell is higher than its surroundings, whereas negative values mean it is lower than its surroundings. TPI values near zero imply flat areas where the slope is near zero or mid-slope areas (Jenness 2013). The integration of topographic variables such as lidar-DEM and TPI could improve detection and change analysis because land cover and land use change generally occurs along topographic gradients (Birhane *et al.* 2019; Liu *et al.* 2020).

Several classification methods, including but not limited to deep learning and machine learning, have been recently used in land cover mapping and change detection analysis (Bai *et al.* 2021; Sefrin *et al.* 2021; Shao *et al.* 2014; Yao *et al.* 2021; Zhao *et al.* 2017; Zhong *et al.* 2021). For example, Sefrin *et al.* (2021) used fully convolutional neural network independently and combined with long short-term memory networks to distinguish land cover changes and misclassifications of deep learning approaches. They found that the multi-temporal sequential information used when fully convolutional neural network was combined with long short-term memory networks outperformed the mono-temporal fully convolutional neural network approach in landcover change detection mapping. Furthermore, Zhao *et al.* (2017) integrated object-based classification with deep learning to improve urban land cover classification. Shao *et al.* (2014) used a machine learning hierarchical semi-supervised support vector machine algorithm to classify landcover in hyperspectral images. They found improved accuracy in landcover detection using hierarchical semi supervised support vector machine technique relative to Kernel fuzzy C-means approach. In addition, Yao *et al.* (2021) explored continuous multi-angle remote sensing data relative to single angle in land cover and use classification. They found improved land cover classification accuracy using continuous multi-angle relative to single angle remote sensing data.

Recent study in Connecticut, United States examined land cover and land use change from 1985 and 2015 using Landsat-derived 30 m land cover maps (Arnold *et al.* 2020). They found a 4.7% increase in development related land covers and corresponding losses to forest and agricultural land. Furthermore, Homer *et al.* (2020) analyzed land cover change patterns from 2001 to 2016 in the Conterminous United States using Landsat series satellite data and ancillary data included but not limited to the National Land Cover Database, DEM, and derivatives such as slope and aspect. They found significant change in the Conterminous United States landscape with about 50% of forest loss. Agriculture areas increased slightly during the study period but there

Department of Agricultural and Environmental Sciences, College of Agriculture, Tennessee State University, Nashville, Tennessee (aclemen1@tnstate.edu).

Contributed by Zhenfeng Shao, July 15, 2021 (sent for review November 4, 2022; reviewed by Bin Hu, Hongping Zhang).

Photogrammetric Engineering & Remote Sensing
Vol. 88, No. 4, April 2022, pp. 243–253.
0099-1112/22/243–253

doi: 10.14358/PERS.21-00042R3

Call for *PE&RS* Special Issue Submissions

Monitoring Earth Hazard with Remote Sensing Techniques

Natural and human disasters are increasingly affecting global communities worldwide in recent decades. With the increasing human population and urbanization, the earth is inevitably more susceptible to manmade hazards. Global warming and its associated environmental instability increase the frequency and severity of the disaster. Rapid Climate change is linked with meteorological events with a high degree of risk probability causing flood disasters. Implementation of proper hazard management such as disaster prevention, disaster preparedness, and adequate disaster relief would reduce the impact of natural disasters. Usage of the convectional earth observation model helps hazard management with a reliable solution but cannot provide early prediction of disaster occurrence, saving people's lives. However, using remote sensing techniques would enable warning systems by building futuristic codes that predict the hazards and warn people on time with greater accuracy. Remote sensing imagery provides a quick method for assessing the variation of hazard impacts, coastal inundation, erosion, and majority affected flood plains using intelligent, visionary technology. The data gathered from sensors provide valuable insights about the spatial phenomena that aid scientists in making accurate decisions about the forecast patterns. Above all satellites, remote sensing is used to detect global environmental problems, explore resources, and monitor disasters by capturing the earth's surface during altered weather conditions. This helps in the early detection of disaster patterns with futuristic mitigation procedures.

The sensors technology captures images of fires, flooding, and volcanic eruption can create a visual impact during the response phase that aids in readiness actions when people are viable to disaster risk. Earth observation systems and GIS helps professionals to make effective project planning with a more accurate analysis. The utilization of various spectral bands such as Visible, infrared, thermal infrared, and synthetic aperture radar provides adequate coverage of environmental patterns and allows technology enhancement to analyze data. Meteorological satellites use High-resolution transmission sensors for cyclone monitoring, intensity assessment, and storm surges. Geo-stationary satellites use global coverage sensors for flood and drought management by collections of multi-date imaginary data for rainfall and river stages. Using its unique spectral signature, it identifies the water standing areas, the sand casting of agricultural lands, and marooned villages to enable hazard recovery plans. SAR sensing system is used to detect forest fires and forest monitoring using microwave techniques to acquire sensory images. There are some challenges about using sensors for hazard prediction where research prospects are needed. As smart sensors use advanced technologies and complex data for prediction, data breaches would lead to misinterpretation of results, increasing the risk to human lives. An adequate skilled workforce is required to analyze the collected sensor data. In the future, integrating IoT and artificial intelligence would create autonomous drones that aid in inspecting the geographical patterns in multi-dimensional views to accelerate high definitions imagery for efficient prediction of results. This special issue enumerates the role of remote sensors for earth hazard predictions and future advancements. We welcome scholars and practitioners of this platform to emphasize this topic and present submissions that fall within the scope of remote sensing techniques for the accurate prediction of environmental hazards.

The topics of interest include:

- Role of Artificial intelligence in generating patterns in sensor data
- Disaster management cycle and it's important in hazard mitigation
- Advantages of geometrics in disaster risk management
- Usage and applications o GIS in flood forecasting
- Advanced Earth observation system tools for project planning
- RadarSat and use cases in detecting oil seeps
- Big data and its uses for accurate data collection in sensors
- Role of climate change in creating environmental risk
- Advancement in satellite sensors for earth's behavioral prediction
- Role of autonomous drones in capturing multispectral images

Deadline for Manuscript Submission

June 5, 2022

Submit your Manuscript to

http://asprs-pers.edmgr.com

Guest Editors

Dr. Priyan Malarvizhi Kumar, mkpriyan@khu.ac.kr and p.malarvizhikumar@ieee.org, *Department of Computer Science and Engineering, Kyung Hee University*, South Korea.

Dr. Fatemeh Afghah, fatemeh.afghah@nau.edu, *School of Informatics, Computing and Cyber Systems, Northern Arizona University.*

Dr. Manimuthu Arunmozhi, arunmozhi.m@ntu.edu.sg, *Cybersecurity Research Center (CYSREN), Nanyang Technological University*, Singapore.

Use of Commercial Satellite Imagery to Monitor Changing Arctic Polygonal Tundra

Amit Hasan, Mahendra Udawalpola, Anna Liljedahl, and Chandi Witharana

Abstract

*Commercial satellite sensors offer the luxury of mapping of individual permafrost features and their change over time. Deep learning convolutional neural nets (*CNNs*) demonstrate a remarkable success in automated image analysis. Inferential strengths of* CNN *models are driven primarily by the quality and volume of hand-labeled training samples. Production of hand-annotated samples is a daunting task. This is particularly true for regional-scale mapping applications, such as permafrost feature detection across the Arctic. Image augmentation is a strategic "data-space" solution to synthetically inflate the size and quality of training samples by transforming the color space or geometric shape or by injecting noise. In this study, we systematically investigate the effectiveness of a spectrum of augmentation methods when applied to* CNN *algorithms to recognize ice-wedge polygons from commercial satellite imagery. Our findings suggest that a list of augmentation methods (such as hue, saturation, and salt and pepper noise) can increase the model performance.*

Introduction

A network of polygonal patterns appears in the tundra due to the cracking and subsequent development of ice wedges. Ice-wedge polygons (IWPs) are one of the most common landforms across the Arctic tundra lowlands. Early studies (Leffingwell 1919) described two major types of IWPs: (1) polygons with elevated blocks or high-centered polygons and (2) polygons with depressed blocks or low-centered polygons. The microtopography associated with IWP controls a multitude of functions of the Arctic ecosystem (Kutzbach *et al.* 2004), such as permafrost and hydrologic dynamics from local to regional scales, due to the linkages between microtopography and the flow and storage of water (Liljedahl *et al.* 2016), vegetation succession (Magnússon *et al.* 2020), and permafrost dynamics (Lara *et al.* 2020). Widespread ice-wedge degradation is transforming low-centered polygons into high-centered polygons in a rapid phase (Steedman *et al.* 2016).

The entire Arctic has been imaged by high-spatial-resolution commercial satellite sensors, producing sheer volumes of data. Imagery archives are quickly morphing to petabyte scale. While studies have been conducted on vegetation dynamics (Verdonen *et al.* 2020), phenology (Zheng *et al.* 2020), vegetation classification (Davidson *et al.* 2016), and spectral and seasonal variation of leaf area index (Juutinen *et al.* 2017), imagery-derived products lag behind. We are in the process of translating these big imagery resources to Arctic science–ready products. Our ongoing research investigates the automated detection of IWPs from commercial satellite imagery.

The successful implementation of deep learning (DL) convolutional neural nets (CNNs) in computer vision applications has received a great deal of interest from the remote sensing community (Ma *et al.* 2019). There has been an upsurge of recent research that exhibits DLCNN applications in a multitude of remote sensing classification problems, such as land use and land cover types of detection (Paoletti *et al.* 2019; Zhang *et al.* 2019), agricultural crop mapping (Zhong *et al.* 2019), feature extraction from remote sensing images (Romero *et al.* 2016), object localization (Long *et al.* 2017), cloud detection (Xie *et al.* 2017), and disaster recognition (Liu & Wu 2016). DLCNNs perform well in terms of object detection (Zhao *et al.* 2019), image segmentation (Rizwan I Haque and Neubert 2020), and semantic object instance segmentation (Lateef and Ruichek 2019). An array of DLCNN architectures have been developed, trained, and tested with different types of imagery. Each of these architectures has its own advantages and disadvantages with respect to computation time and resources. Among many others, Mask R-CNN, U-Net, and Deeplab V3+ stand out as superior methods in semantic object instance segmentation. Researchers used Deeplab V3+ with the Pascal VOC data set and achieved 89% intersection over union (IoU). In a separate biological image segmentation data set, the U-Net model achieved a total of 85.5% IoU (Karimov *et al.* 2019). There is an increasing interest in the application of the Mask R-CNN model for Earth science applications (Su *et al.* 2019; Bhuiyan *et al.* 2020; Carvalho *et al.* 2021; Mahmoud *et al.* 2020; Zabawa *et al.* 2020; Zuo *et al.* 2020). Previous studies have shown promising results found by the implementation of DLCNN with commercial satellite imagery (Zhang *et al.* 2018; Bhuiyan *et al.* 2020; Witharana *et al.* 2020). By design, inferential strengths of CNN models are fueled largely by the quality and volume of hand-labeled training data. Production of hand-annotated samples is a daunting task. This is particularly true for regional-scale mapping applications, such as permafrost feature detection across the Arctic, where landscape complexity would spontaneously inflate the semantic complexity of submeter-resolution imagery. Additionally, image dimensions, multispectral channels, imaging conditions, and seasonality, coupled with multi-scale organization of geo-objects, pose extra challenges on the generalizability of DLCNN models. Image augmentation is a strategic "data-space" solution to synthetically inflate the size and quality of training samples without additional investments on hand annotations. A plethora of augmentation methods have been proposed under the auspices of two general categories: data warping and oversampling (Shorten and Khoshgoftaar 2019). The performance of image augmentation methods depends largely on the image recognition problem on hand and the characteristics of the underlying data. Researchers have used color augmentation techniques for skin lesion segmentation and classification (Galdran *et al.* 2017), geometric transformation with chest X-ray for the screening of COVID-19 (Elgendi *et al.* 2021), and noise injection techniques for plant leaf disease detection (Arun Pandian *et al.* 2019).

In this study, we have investigated the efficacy of 17 augmentation methods in relation to IWP detection. We relied on the Mask R-CNN algorithm as the base model in the training and the prediction of IWPs. The Mask R-CNN model itself has a lot of room to modify and tweak the default parameters (He *et al.* 2017). The backbone of the model is a convolutional neural network. This can be changed to different types of CNN models; we used the ResNet-50 structure (He *et al.* 2015) as the backbone. To initialize the model, we have practiced the transfer learning approach. In this approach, the model is already trained based on another hand-labeled data set. Our backbone was pretrained based on

Amit Hasan, Mahendra Udawalpola, and Chandi Witharana are with the University of Connecticut, Storrs, CT 06269 (amit.hasan@uconn.edu).

Anna Liljedahl is with the Woodwell Climate Research Center, Falmouth, MA 02540.

Contributed by Alper Yilmaz, August 30, 2021 (sent for review August 30, 2021).

Photogrammetric Engineering & Remote Sensing
Vol. 88, No. 4, April 2022, pp. 255–262.
0099-1112/22/255–262

doi: 10.14358/PERS.21-00061R2

An Evaluation of Pan-Sharpening Methods for *SuperView-1* Satellite Imagery

Lei Zhang, Bowen Wen, Ming Zhang, Qiongqiong Lan, and Qian Wang

Abstract

*At present, little research focuses on the application of pan-sharpening methods to SuperView-1 satellite imagery. There is a lack of suitability assessment for existing pan-sharpening methods applied to SuperView-1 images. This study proposes an evaluation method that integrates visual evaluation, spectral analysis of typical objects, and quantitative indicators to evaluate the advantages of different pan-sharpening methods in different scenes of SuperView-1 imagery. Four scenes (urban areas, farmland, sparse vegetation, mixed surfaces) are selected to evaluate eight typical pan-sharpening methods (Brovey, principal component analysis (*PCA*), Gram-Schmidt (*GS*), band-dependent spatial-detail (*BDSD*), high-pass filtering (*HPF*), smoothing filter-based intensity modulation (*SFIM*), modulation transfer function-generalized Laplacian pyramid (*MTF-GLP*),* MTF-GLP*-high pass modulation (*MTF-GLP-HPM*). The results show that the suitability of each pan-sharpening method is different in various scenes.* PCA*, Brovey, and* GS *distort the spectral information greatly, and the stability of the pan-sharpening results in different scenes which are poor.* BDSD *has strong stability and can better balance the relationship between spectral distortion and spatial distortion in different scenes. The multi-resolution analysis method has better applicability and stability for SuperView-1 imagery, among which* MTF-GLP *and* MTF-GLP-HPM *perform better in the pan-sharpening results. This study provides a reference for the selection of pan-sharpening methods for SuperView-1 imagery in different application fields.*

Introduction

The rapid development of optical sensing technology has brought abundant remote sensing data with increasing resolution. Due to the constraint between spatial resolution and spectral resolution, the spatial resolution of multispectral images (MS) in satellite data is lower than that of panchromatic images (PAN). Pan-sharpening technology can fuse multispectral and panchromatic images in the same scene to generate high-resolution multispectral images. The fused image not only retains rich spectral information, but also highlights more spatial details. Vivone *et al.* (2021) analyzed in detail the latest developments in MS pan-sharpening (Vivone *et al.* 2021). Javan *et al.* (2021) reviewed 41 pan-sharpening methods and applied them to high-resolution images for testing and comparison (Javan *et al.* 2021). Meng *et al.* (2019) provided a comprehensive review of pan-sharpening methods, and evaluated existing methods based on meta-analysis (Meng *et al.* 2019). Vivone *et al.* (2015) described and extensively compared some of the most advanced pan-sharpening methods (Vivone *et al.* 2015). Ghassemian (2016) reviewed pixel-level pan-sharpening methods and discussed the assessment of fused results (Ghassemian 2016). Pan-sharpening methods realize the complementary advantages of different imagery, satisfy the ever-evolving application requirements, and play an important role in application fields such as image recognition and classification (Yuhendra *et al.* 2011).

Currently, pan-sharpening methods can be classified into three categories: component substitution (CS), multi-resolution analysis (MRA), and model-based methods (Vivone *et al.* 2021). The CS methods extract the component that determines the spatial resolution of the multispectral image and improve the resolution of the multispectral image by replacing this component with the panchromatic image. The classic CS methods include Brovey (Dong *et al.* 2021; Mandhare *et al.* 2013; Sarp 2014), Principal Component Analysis (PCA) (Ghadjati *et al.* 2019; Tambe *et al.* 2021; Wang *et al.* 2016), Gram-Schmidt (GS) (Candra 2013; Tabib Mahmoudi and Karami 2020; Yilmaz *et al.* 2020), Band-Dependent Spatial-Detail (BDSD) (Imani 2018; Vivone 2019; Zhong *et al.* 2017), etc. The CS methods are easy to implement, but the fusion results have the problem of spectral distortion. Wang *et al.* (2014) used the particle swarm optimization model to propose a new pan-sharpening method based on adaptive component substitution (Wang *et al.* 2014). Li *et al.* (2020) improved the component substitution pan-sharpening method by refining the spatial detail (Li *et al.* 2020). The MRA methods perform image transformation on the multi-source images, extract the spatial detail from the panchromatic image, and add it to the multispectral image to obtain the fused image. The classic MRA methods include High-Pass Filtering (HPF) (Gangkofner *et al.* 2007; Metwalli *et al.* 2010; Pushparaj and Hedge 2017), Smoothing Filter-Based Intensity Modulation (SFIM) (Alcaras *et al.* 2021; Liu 2000), modulation transfer function -generalized Laplacian pyramid (MTF-GLP) (Aiazzi *et al.* 2006), MTF-GLP with high pass modulation (MTF-GLP-HPM) (Lee and Lee 2009), etc. The MRA methods can better control the spectral distortion. The model-based methods assume that the low-resolution multispectral image is obtained from high-resolution multispectral image through down-sampling or other operations. They establish the relationship model between high-resolution multispectral image and low-resolution multispectral image and panchromatic image, express the model with energy functional, and then obtain the fused image by optimizing the model. Wang *et al.* (2019) proposed a regularized model-based pan-sharpening method to reduce the impact of local dissimilarities (Wang *et al.* 2019). Guo *et al.* (2020) developed a new model-based pan-sharpening method based on Bayesian theory (Guo *et al.* 2020). The model-based methods have high spectral fidelity, but their computational complexity leads to unsatisfactory time efficiency.

Most scholars used quantitative indicators to evaluate the fusion results of pan-sharpening methods. Commonly used quantitative indicators include Spectral Angle Mapper (SAM) (Alparone *et al.* 2008; Pandit and Bhiwani 2015), Erreur Relative Globale Adimensionnelle de Synthese (ERGAS) (Alparone *et al.* 2008; Pandit and Bhiwani 2015), Spatial Correlation Coefficient (SCC) (Pushparaj and Hegde 2017),

Lei Zhang is with the School of Remote Sensing and Information Engineering, Wuhan University, Wuhan 430079, China.

Bowen Wen and Ming Zhang are with the School of Resources and Environmental Engineering, Wuhan University of Technology, Wuhan 430070, China (zhangming_88@whut.edu.cn).

Qiongqiong Lan is with the China Centre for Resources Satellite Data and Application, Beijing 100094, China.

Qian Wang is with the School of Geographic and Environmental Sciences, Tianjin Normal University, Tianjin 300387, China.

Contributed by Sidike Paheding, August 23, 2021 (sent for review October 29, 2021; reviewed by Francisco Javier Ariza-Lopez, Jianyu Gu, Jiaming Wang).

Photogrammetric Engineering & Remote Sensing
Vol. 88, No. 4, April 2022, pp. 263–269.
0099-1112/22/263–269

doi: 10.14358/PERS.21-00051R3

Call for Submissions

AI-Based Environmental Monitoring with UAV Systems

Photogrammetric Engineering and Remote Sensing (*PE&RS*) is seeking submissions for a special issue on AI-Based Environmental Monitoring with UAV Systems.

Global warming and climate change have become the most important factor threatening the world. Climate change results in dramatical environmental hazards and threatens the planet and human life. A wide variety of policies have been proposed to decrease the effects of global warming and climate change. The most important one is the Paris Agreement which aims to limit global warming to well below two degrees Celcius. Many countries have formulated long term low greenhouse gas emission development strategies related to the Paris Agreement which aimed to meet the essential strategies addressing issues with climate change, environmental protection and low carbon.

The astonishing developments on unmanned aerial vehicle (UAV) systems and artificial intelligence (AI) technologies enables a great opportunity to monitor the environment and propose reliable solutions to restore and preserve the planet and human health.

Data acquisition and processing paradigm has been changed as a result of technological developments. It is obvious that new solutions, innovative approaches will make significant contributions to solve the problems which our planet is facing. UAV data can be collected by various platforms (planes or helicopters, fixed wing systems, drones) and sensors for earth observation and sustainable environmental monitoring which are also utilized by the United Nations to support the delivery of its mandates, resolutions, and activities.

UAV based earth observation data and AI techniques have a wide range of applications such as risk management, disaster monitoring and assessment, environmental impact evaluation and restoration, monitoring agriculture and food cycles, urban analysis, digital twin and smart city applications and providing increased situation awareness. This growth of widely available UAV data associated with the exponential increase in digital computing power, machine learning and artificial intelligence plays a key role in the environmental monitoring and solution generation of geospatial information for the benefit of humans and the planet.

The proposed special issue aims to contributes ASPRS's key mission on 'Simplify and promote the use of image-based geospatial technologies for the end-user', 'Promote collaboration between end users and geospatial experts to match data and technology to applications and solutions' and 'promote the transfer of geospatial data and information technology to developing nations' by serving as an innovative knowledge exchange platform for authors from the globe to deliberate on the latest advancements, state-of-the-art developments and solutions that can help the community to solve many real-world challenges on the topic of "*AI-Based Environmental Monitoring with UAV Systems*."

This special issue aims to bring researchers to share knowledge and their expertise about state-of-art developments and contribute to the goal of a livable world by integrating human creativity with UAV and AI technologies for environmental monitoring to combat global threats on ecosystems. We wish to discuss the latest developments, opportunities and challenges that can solve many real-world challenges in environmental monitoring including but not limited to:

- AI-Based UAV and GIS Applications
- AI-Based Object Detection and Recognition from UAV Imagery
- AI-Based Digital Twin Applications
- AI-Based Smart City Applications

Papers must be original contributions, not previously published or submitted to other journals. Submissions based on previous published or submitted conference papers may be considered provided they are considerably improved and extended. Papers must follow the instructions for authors at http://asprs-pers.edmgr.com/.

Deadline for Manuscript Submission
May 1, 2022

Submit your Manuscript to
http://asprs-pers.edmgr.com

Guest Editor
Tolga Bakirman, PhD, Y*ildiz Technical University*, Turkey
Dr. Tolga Bakirman. bakirman@yildiz.edu.tr. is an assistant professor at Yildiz Technical University in the Department of Geomatic Engineering.

Floating Solar Park Impacts Urban Land Surface Temperature Distribution Pattern

Bo Yingjie, Li Guoqing, Zeng Yelong, and Liu Zhe

Abstract

In recent years, the global photovoltaic industry has developed rapidly. It is significant for evaluating the impact of large-scale solar parks on the environment for the sustainable development of the photovoltaic industry. At present, researchers have paid attention to changes in the local thermal environment caused by solar parks. As a new type of solar park, the influence of floating solar parks on urban land surface temperature distribution patterns is still unclear. In this article, we (1) take the floating solar parks in Huainan City, China, as the study area; (2) calculate the land surface temperature (LST) of the study area and its adjacent areas by using Landsat 8 remote sensing data and the radiation transfer equation method; and (3) judge the influence of solar parks on the distribution pattern of LST. On this basis, we analyzed the influence range and seasonal differences of floating solar parks on LST. Our results revealed that, first, the floating solar park has a warming effect in the summer and winter, and the warming area is concentrated mainly within 200 m of the photovoltaic panels' coverage area. Second, during the construction phase and after the completion of the floating solar parks, the average monthly LST of the solar panels is generally higher than the water, and the average annual temperature increase in the above two stages is 3.26°C and 4.50°C, respectively. The change of floating solar parks on urban LST distribution patterns may impact the local ecosystem. In the future, it is necessary to consider the impact of floating solar parks on local LST during the construction of floating solar parks.

Introduction

Unlike fossil energy sources, such as coal, oil, and natural gas, solar energy has the advantages of cleanness, safety, sustainable regeneration, and convenient access (Parida *et al.* 2011). The global development of photovoltaic power generation has been expected to change energy production and consumption based on fossil energy since the industrial revolution and effectively alleviate the energy crisis, global carbon emissions, and environmental pollution (Kerr 2010; Schmela *et al.* 2016; Forstner *et al.* 2018; Raturi 2019). In recent years, China's photovoltaic power generation has developed rapidly under the encouragement of diversified policies. In 2013 and 2015, China successively surpassed Italy and Germany to become the country with the largest installed capacity of photovoltaic power generation worldwide and has been leading up to now (Li *et al.* 2016; Li and Liu 2020; Raturi 2020). By the end of 2020, the cumulative installed capacity of photovoltaic power generation in China reached 253 GW, an increase of 23.5% year on year (Wong 2021).

However, the construction of large-scale solar park projects will inevitably impact the region's local land, ecology, and energy cycle (Tawalbeh *et al.* 2021). The impact of large-scale solar parks on the environment during construction is similar to that of other industrial manufacturing processes. For example, engineering activities, such as land leveling and installing solar panels, directly change the original soil, vegetation, topography, and land use status. These activities further change their original form and even destroy the stable structure of the original environmental elements, resulting in land disturbance, vegetation destruction, and soil erosion (Li *et al.* 2017; Choi *et al.* 2020; Tawalbeh *et al.* 2021; Yue *et al.* 2021). After the solar parks are built, solar panels will absorb short-wave radiation to convert solar energy into electric energy and at the same time radiate long-wave radiation outward. This will change the energy flow mode of the local surface and affect the power generation efficiency of solar panels, local climate, and energy cycle of the ecosystem (Yang *et al.* 2015, 2017; Fan and Wang 2020; Pimentel Da Silva *et al.* 2020). Using remote sensing to analyze land surface temperature (LST) change can effectively judge the influence of large-scale solar parks on the energy cycle (Liou *et al.* 2017; Shao *et al.* 2019a; Wang *et al.* 2021). Studies have shown that the daily average LST around the solar park is reduced by 0.53°C (Zhang and Xu 2020). However, in the desert and Gobi, the cooling effect of the solar park is more obvious, and the average annual decrease of LST can reach 4°C with an influence range of about 100–600 m (Chang *et al.* 2018; Liu *et al.* 2019; Li and Liu 2020).

In recent years, with the continuous expansion of the scale of the photovoltaic industry, the water surface in cities and towns has become one of the available areas for building solar parks, which has explored a new model for the development of global new energy and cleaner production (Sahu *et al.* 2016). However, there is no effective analysis to judge the influence range and variation range of the floating solar parks on the local temperature due to the significant difference between the underlying surface of the floating solar parks and the solar land parks. Because of this, we take the floating solar parks in Huainan City, Anhui Province, China, as the research area and use remote sensing data to judge the influence of the floating solar parks on the surrounding LST. Our research objectives are as follows:

1. Based on Google Earth Engine and *Landsat 8* remote sensing images, the radiation transfer equation method constructed LST data sets of floating solar parks and their adjacent areas.
2. Using LST data sets, we can judge the influence of solar parks on the spatial distribution pattern of LST.
3. On this basis, the spatial range and warming or cooling range of the solar parks on the LST is obtained.

Data and Methods

Study Area

The study area is located in Huainan City, Anhui Province. The climate in this area is warm temperate semi-humid monsoon, with high-temperature and rainy summers and cold and dry winters. The annual sunshine hours are 2000 hours, and the annual solar radiation is 4,800 MJ/m^2 (1990–2020, data from Bengbu and Lu'an meteorological stations).

Bo Yingjie, Li Guoqing, and Liu Zhe are with Ludong University, Institute of Resources and Environmental Engineering, Yantai 264025, China (corresponding author, Li Guoqing: ligqing@foxmail.com).

Zeng Yelong is with the Aerospace Information Research Institute, Beijing, China, 100101; the Chinese Academy of Sciences, Beijing 100101, China; and the State Key Laboratory of Remote Sensing Science, Beijing 100101, China.

Contributed by Zhenfeng Shao, October 8, 2021 (sent for review November 22, 2021; reviewed by Linjing Zhang, Neema S S Sumari).

Photogrammetric Engineering & Remote Sensing
Vol. 88, No. 4, April 2022, pp. 271–278.
0099-1112/22/271–278

doi: 10.14358/PERS.21-00083R2

WHO'S WHO IN ASPRS

Founded in 1934, the American Society for Photogrammetry and Remote Sensing (ASPRS) is a scientific association serving thousands of professional members around the world. Our mission is to advance knowledge and improve understanding of mapping sciences to promote the responsible applications of photogrammetry, remote sensing, geographic information systems (GIS) and supporting technologies.

BOARD OF DIRECTORS

BOARD OFFICERS

President
Christopher Parrish, Ph.D
Oregon State University

President-Elect
Lorraine B. Amenda, PLS, CP
Towill, Inc.

Vice President
Bandana Kar
Oak Ridge National Lab

Past President
Jason M. Stoker, Ph.D,
U.S. Geological Survey

Treasurer
Stewart Walker, Ph.D.
photogrammetry4u

Secretary
Harold Rempel
ESP Associates, Inc.

COUNCIL OFFICERS

ASPRS has six councils. To learn more, visit https://www.asprs.org/Councils.html.

Sustaining Members Council
Chair: Ryan Bowe
Deputy Chair: Melissa Martin

Technical Division Directors Council
Chair: Bill Swope
Deputy Chair: Hope Morgan

Standing Committee Chairs Council
Chair: David Stolarz
Deputy Chair: TBA

Early-Career Professionals Council
Chair: Madeline Stewart
Deputy Chair: Kyle Knapp

Region Officers Council
Chair: Demetrio Zourarakis
Deputy Chair: Jason Krueger

Student Advisory Council
Chair: Lauren McKinney-Wise
Deputy Chair: Oscar Duran

TECHNICAL DIVISION OFFICERS

ASPRS has seven professional divisions. To learn more, visit https://www.asprs.org/Divisions.html.

Geographic Information Systems Division
Director: Denise Theunissen
Assistant Director: Jin Lee

Lidar Division
Director: Ajit Sampath
Assistant Director: Mat Bethel

Photogrammetric Applications Division
Director: Ben Wilkinson
Assistant Director: Hank Theiss

Primary Data Acquisition Division
Director: Greg Stensaas
Assistant Director: Srini Dharmapuri

Professional Practice Division
Director: Bill Swope
Assistant Director: Hope Morgan

Remote Sensing Applications Division
Director: Amr Abd-Ehrahman
Assistant Director: Tao Liu

Unmanned Autonomous Systems (UAS)
Director: Jacob Lopez
Assistant Director: Bahram Salehi

REGION PRESIDENTS

ASPRS has 13 regions to serve the United States. To learn more, visit https://www.asprs.org/regions.html.

Alaska Region

Cascadia Region
Robert Hariston-Porter

Eastern Great Lakes Region
Michael Joos, CP, GISP

Florida Region
Xan Fredericks

Heartland Region
Whit Lynn

Intermountain Region
Robert T. Pack

Mid-South Region
David Hughes

Northeast Region

North Atlantic Region

Pacific Southwest Region
John Erickson, PLS, CP

Potomac Region
Dave Lasko

Rocky Mountain Region

Western Great Lakes Region
Adam Smith

SUSTAININGMEMBERS

ACI USA Inc.
Weston, Florida
https://acicorporation.com/
Member Since: 2/2018

Aerial Services, Inc.
Cedar Falls, Iowa
www.AerialServicesInc.com
Member Since: 5/2001

Airworks Solutions Inc.
Boston, Massachusetts
Member Since: 3/2022

Applanix
Richmond Hill, Ontario, Canada
http://www.applanix.com
Member Since: 7/1997

Ayres Associates
Madison, Wisconsin
www.AyresAssociates.com
Member Since: 1/1953

Dewberry
Fairfax, Virginia
www.dewberry.com
Member Since: 1/1985

Environmental Research Incorporated
Linden, Virginia
www.eri.us.com
Member Since: 8/2008

Esri
Redlands, California
www.esri.com
Member Since: 1/1987

GeoCue Group
Madison, Alabama
http://www.geocue.com
Member Since: 10/2003

Geographic Imperatives LLC
Centennial, Colorado
Member Since: 12/2020

GeoWing Mapping, Inc.
Richmond, California
www.geowingmapping.com
Member Since: 12/2016

Halff Associates, Inc.
Richardson, Texas
www.halff.com
Member Since: 8/2021

Keystone Aerial Surveys, Inc.
Philadelphia, Pennsylvania
www.kasurveys.com
Member Since: 1/1985

Kucera International
Willoughby, Ohio
www.kucerainternational.com
Member Since: 1/1992

L3Harris Technologies
Broomfield, Colorado
www.l3harris.com
Member Since: 6/2008

Merrick & Company
Greenwood Village, Colorado
www.merrick.com/gis
Member Since: 4/1995

NV5 Geospatial
Sheboygan Falls, Wisconsin
www.quantumspatial.com
Member Since: 1/1974

Pickett and Associates, Inc.
Bartow, Florida
www.pickettusa.com
Member Since: 4/2007

Riegl USA, Inc.
Orlando, Florida
www.rieglusa.com
Member Since: 11/2004

Robinson Aerial Surveys, Inc.(RAS)
Hackettstown, New Jersey
www.robinsonaerial.com
Member Since: 1/1954

Sanborn Map Company
Colorado Springs, Colorado
www.sanborn.com
Member Since: 10/1984

Scorpius Imagery Inc.
Newark, Delaware
aerial@scorpiusimagery.com
Member Since: 6/2021

Surdex Corporation
Chesterfield, Missouri
www.surdex.com
Member Since: 12/2011

Surveying And Mapping, LLC (SAM)
Austin, Texas
www.sam.biz
Member Since: 12/2005

T3 Global Strategies, Inc.
Bridgeville, Pennsylvania
https://t3gs.com/
Member Since: 6/2020

Terra Remote Sensing (USA) Inc.
Bellevue, Washington
www.terraremote.com
Member Since: 11/2016

Towill, Inc.
San Francisco, California
www.towill.com
Member Since: 1/1952

Woolpert LLP
Dayton, Ohio
www.woolpert.com
Member Since: 1/1985

SUSTAININGMEMBER**BENEFITS**

Membership

- ✓ Provides a means for dissemination of new information
- ✓ Encourages an exchange of ideas and communication
- ✓ Offers prime exposure for companies

Benefits of an ASPRS Membership

- Complimentary and discounted Employee Membership*
- E-mail blast to full ASPRS membership*
- Professional Certification Application fee discount for any employee
- Member price for ASPRS publications
- Discount on group registration to ASPRS virtual conferences
- Sustaining Member company listing in ASPRS directory/website
- Hot link to company website from Sustaining Member company listing page on ASPRS website
- Press Release Priority Listing in *PE&RS* Industry News
- Priority publishing of Highlight Articles in *PE&RS* plus, 20% discount off cover fee
- Discount on *PE&RS* advertising
- Exhibit discounts at ASPRS sponsored conferences (exception ASPRS/ILMF)
- Free training webinar registrations per year*
- Discount on additional training webinar registrations for employees
- Discount for each new SMC member brought on board (Discount for first year only)

*quantity depends on membership level

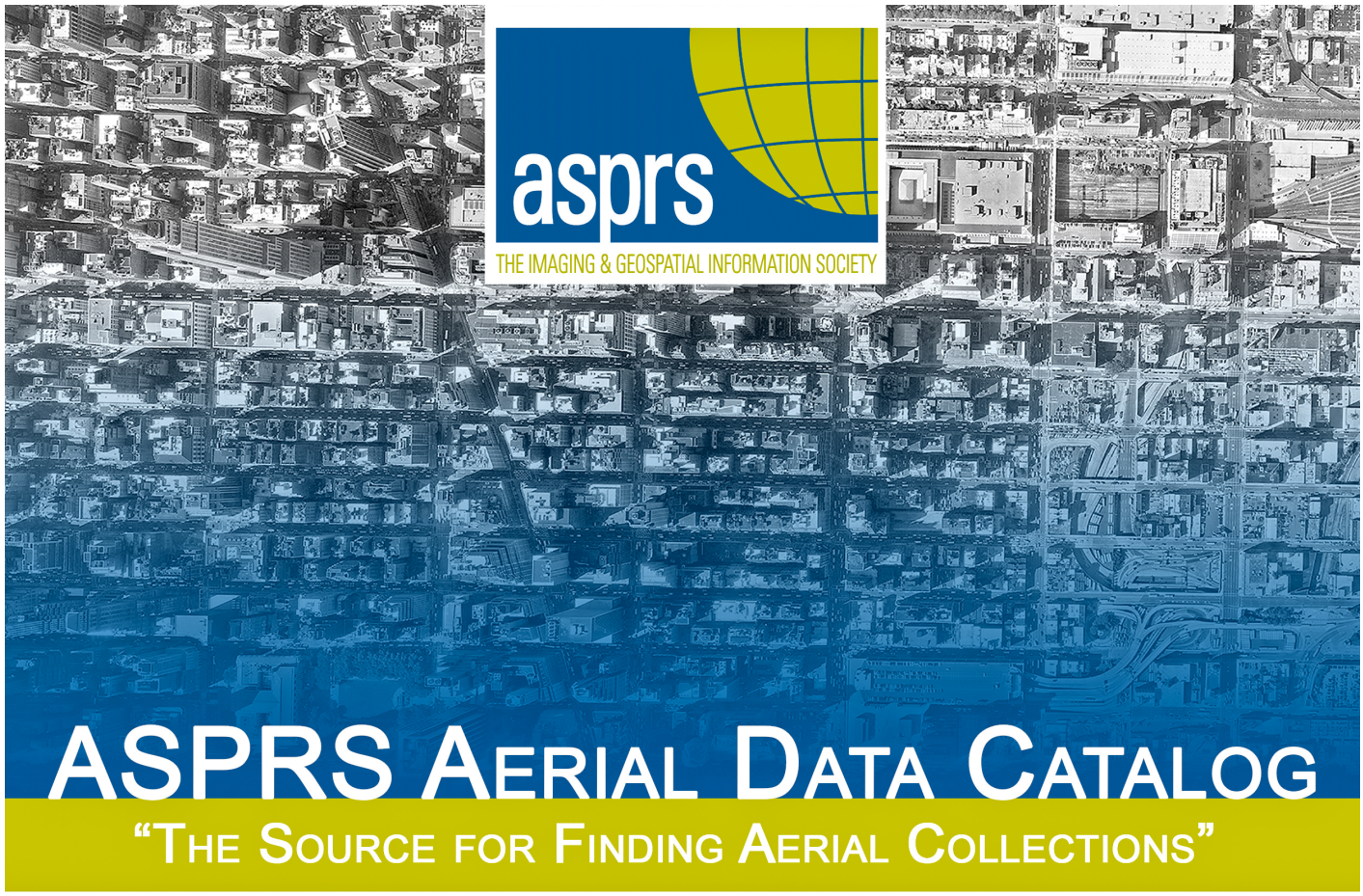

asprs
THE IMAGING & GEOSPATIAL INFORMATION SOCIETY

ASPRS Aerial Data Catalog

"The Source for Finding Aerial Collections"

http://dpac.asprs.org

The ASPRS Aerial Data Catalog is a tool allowing owners of aerial photography to list details and contact information about individual collections.

By providing this free and open metadata catalog with no commercial intrests, the Data Preservation and Archiving Committee (DPAC) aims to provide a definitive metadata resource for all users in the geospatial community to locate previously unkown imagery.

DPAC hopes this Catalog will contribute to the protection and preservation of aerial photography around the world!

ASPRS Members: We Need Your Help!
There are three ways to get involved

1 USE — Use the catalog to browse over 5,000 entries from all 50 states and many countries. Millions of frames from as early as 1924!

2 SUPPLY — Caretakers of collections, with or without metadata, should contact DPAC to add their datasets to the catolog free of charge!

3 TELL — Spread the word about the catalog! New users and data collections are key to making this a useful tool for the community!

For More Details or To Get Involved Contact:

David Ruiz • druiz@quantumspatial.com • 510-834-2001 OR David Day • dday@kasurveys.com • 215-677-3119